An Introduction to Multi-Anvil Techniques

Charles E Lesher
UC Davis

2005 COMPRES Multi-Anvil Workshop
March 1-3, GSECARS - APS

OUTLINE

- Types of multianvil systems
- Design considerations
- Importance of gasketing
- Cell assemblies
- Pressure generation
- Heat generation
- Calibration

Multianvil Systems

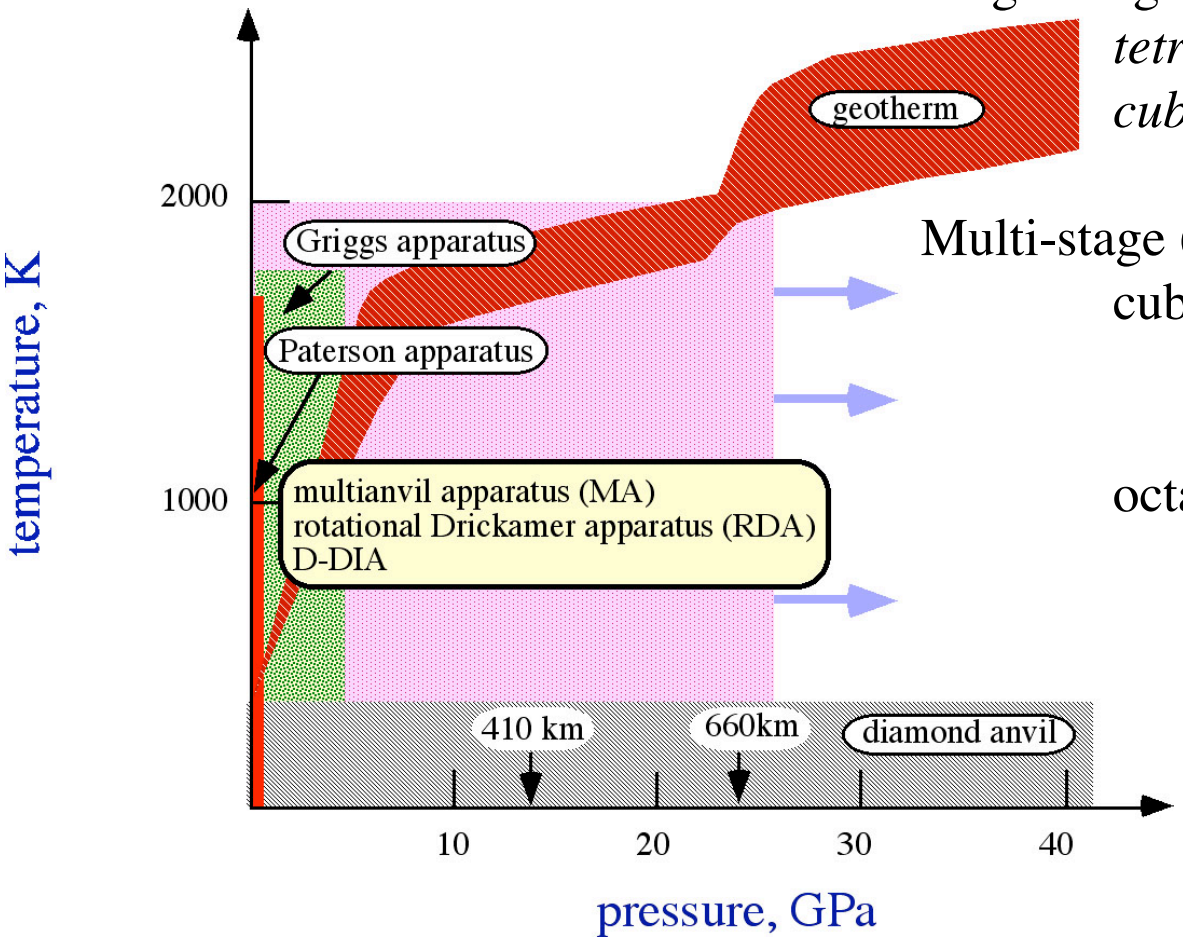

Single-stage (individual rams)

tetrahedral

cubic

Multi-stage (sliding system/guide blocks)

cubic cells

DIA

cylindrical (Getting module)

octahedral cells

split-sphere

DIA

cylindrical (Walker mdoule)

split cylinder (Tcup, T-25)

Single-stage multianvil systems

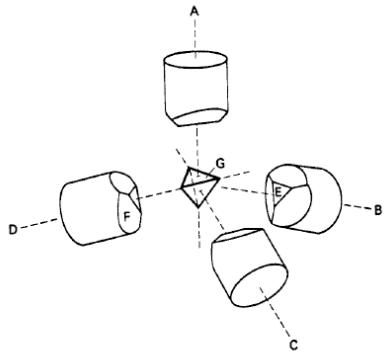

Fig. 2.26. Cluster of tetrahedral anvils.

Single-stage multianvil systems

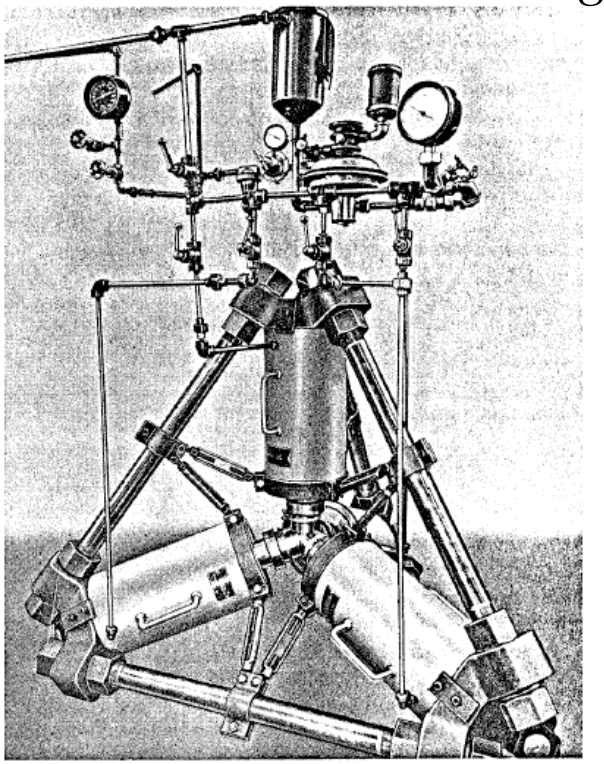

Fig. 2.25. The original tetrahedral press.

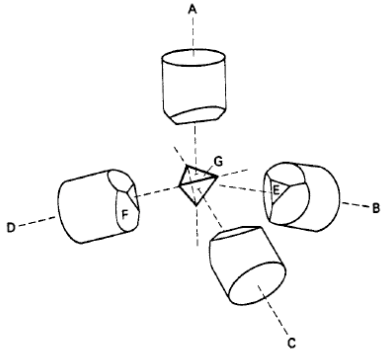

Fig. 2.26. Cluster of tetrahedral anvils.

H. Tracy Hall Foundation

Single-stage multianvil systems

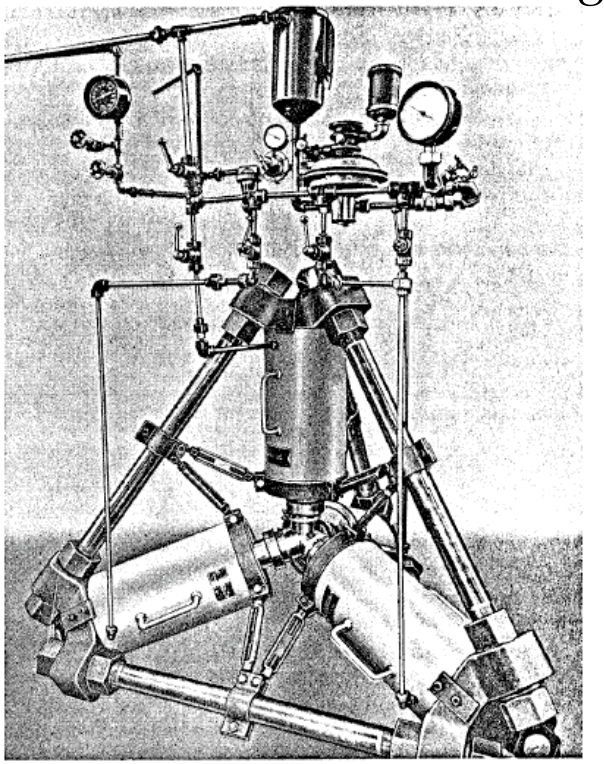

Fig. 2.25. The original tetrahedral press.

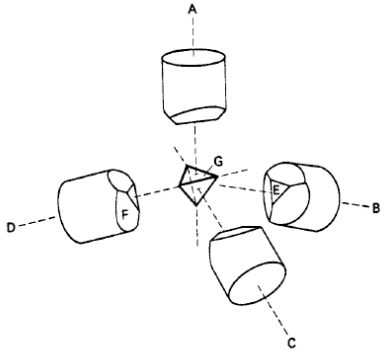

Fig. 2.26. Cluster of tetrahedral anvils.

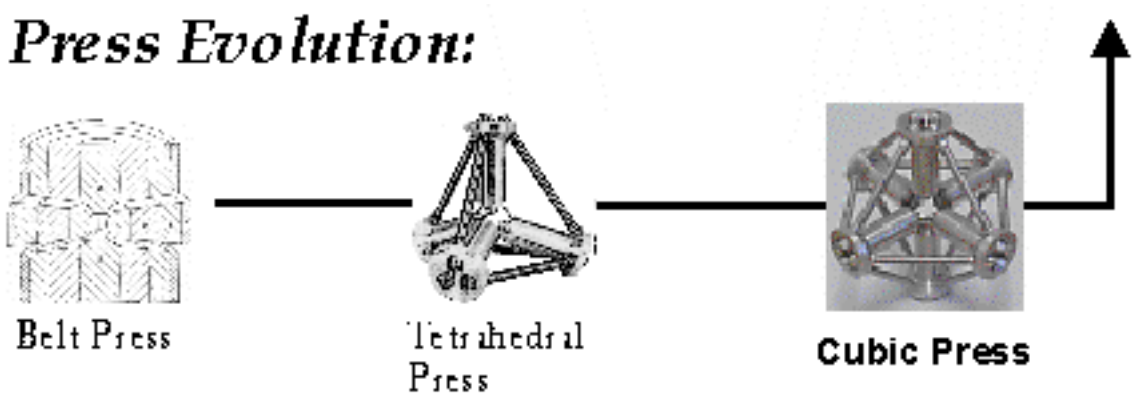

H. Tracy Hall Foundation

Single-stage multianvil systems

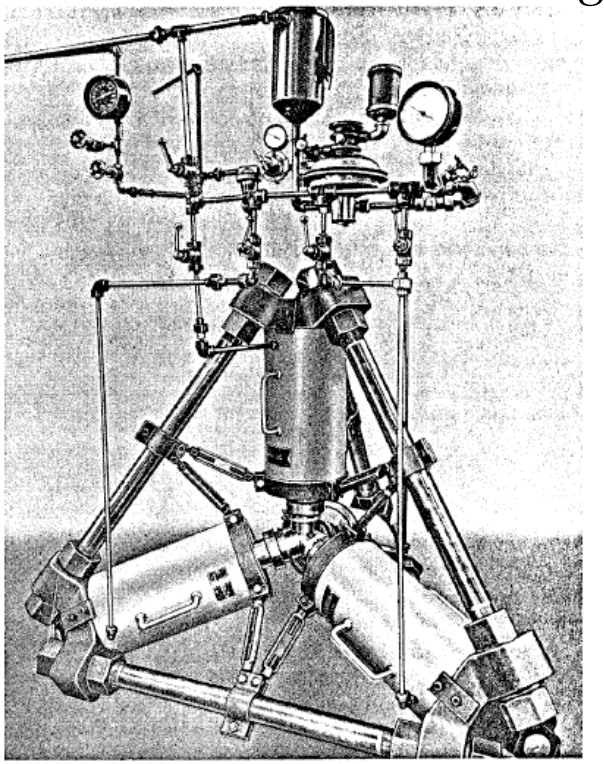

Fig. 2.25. The original tetrahedral press.

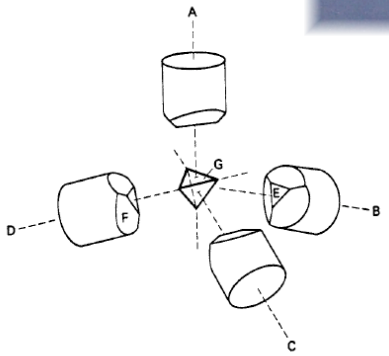

Fig. 2.26. Cluster of tetrahedral anvils.

NovaDiamonds

Press Evolution:

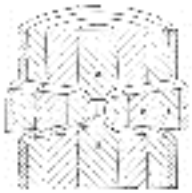

Belt Press

Tetrahedral Press

Cubic Press

H. Tracy Hall Foundation

Multi-stage multianvil systems

Split-sphere apparatus

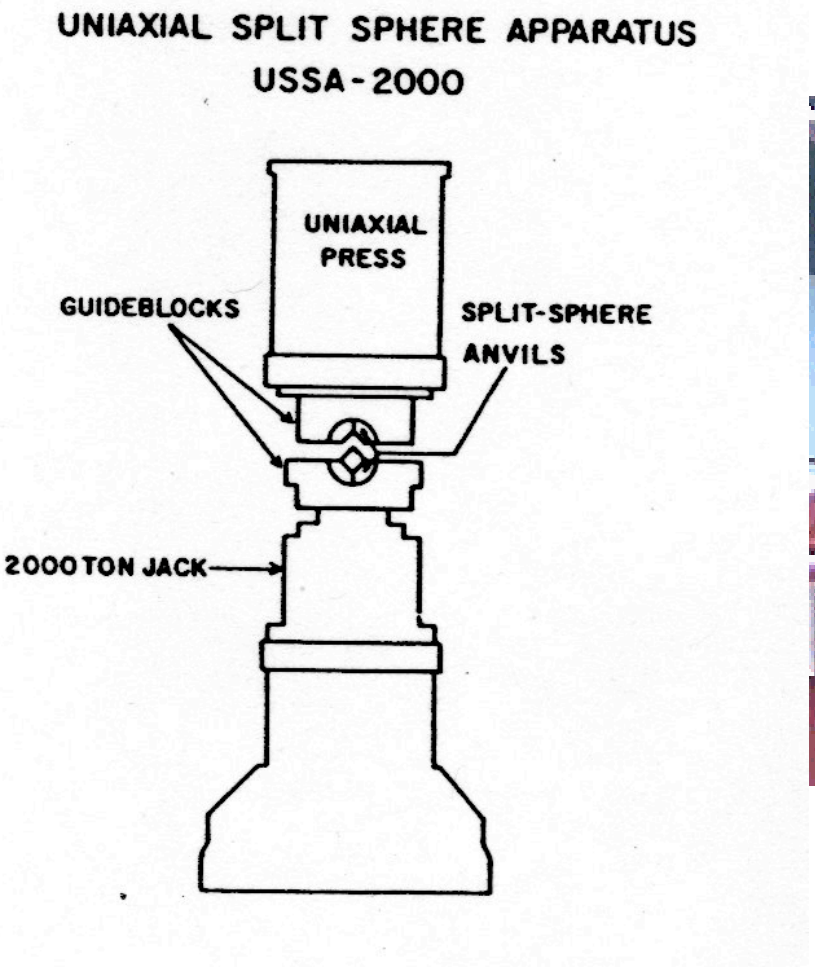

Sumitomo 2000-Ton Press (SUNY-Stony Brook)

Kawai- type (6-8)

First stage:
6 spherical anvils

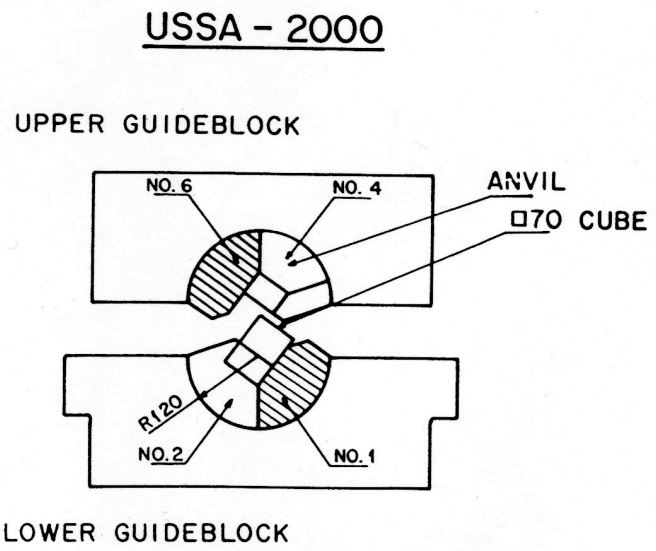

Figure 1
Schematic diagrams for 2000-ton uniaxial split-sphere apparatus (USSA–2000). (a) Hydraulic press with guideblocks and split-sphere anvils in place. (b) Details of the first-stage spherical steel anvils in the guideblocks. (c) Second-stage with the assembly of eight tungsten carbide cubic anvils of truncation edge length (TEL = *a*) which compress an octahedral pressure medium.

Second stage:
8 truncated cubic anvils

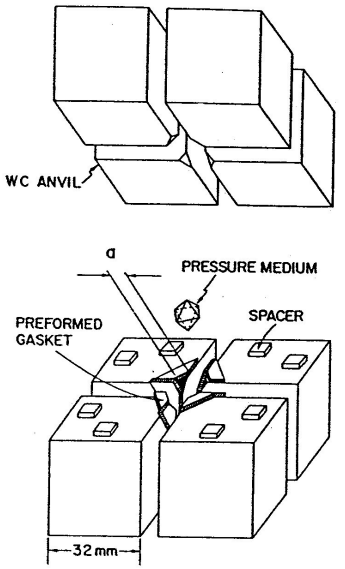

Figure 4. Second stage of the USSA-2000 with the assembly of eight tungsten carbide cubic anvils of truncation edge length (a) which compress an octahedral pressure medium (modified after Sawamoto, 1986).

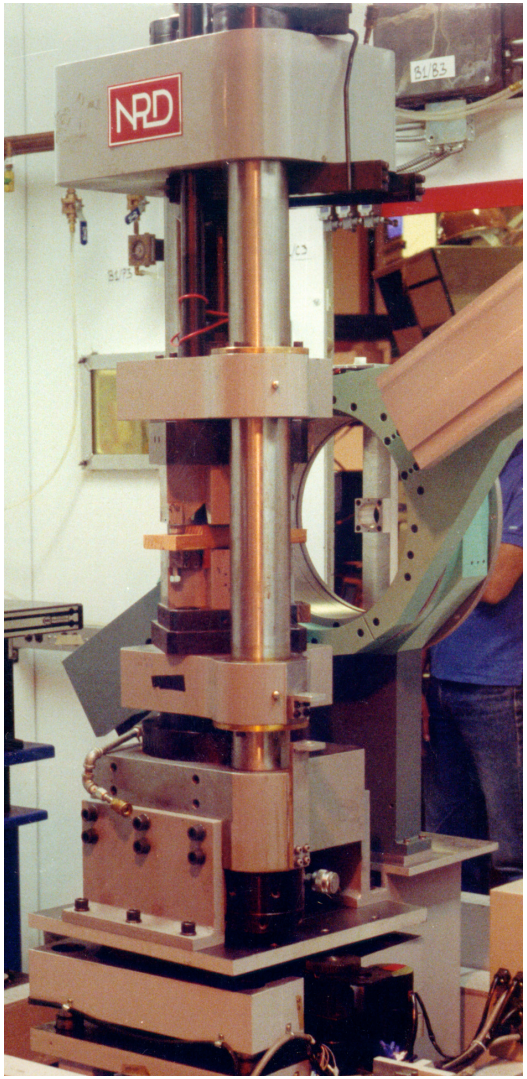

SAM85
at X17B2 (NSLS)

DIA apparatus

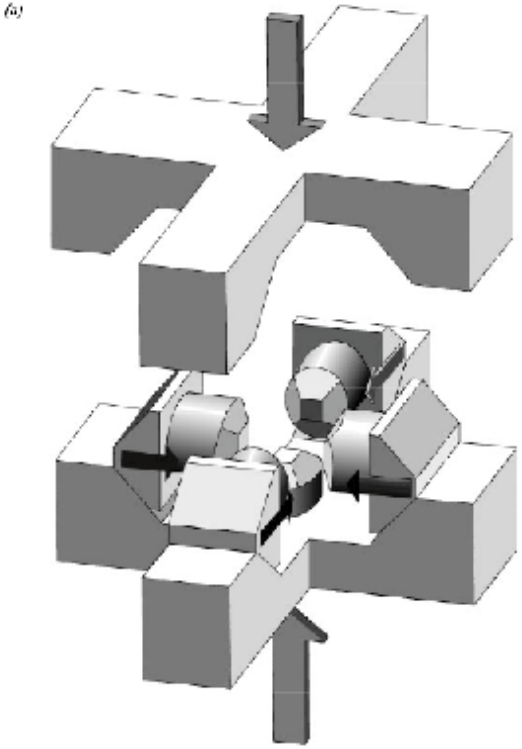

8-6

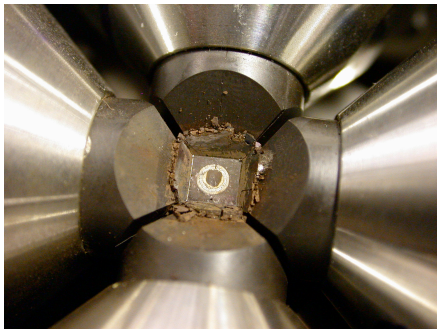

Cubic cell

8-6-8

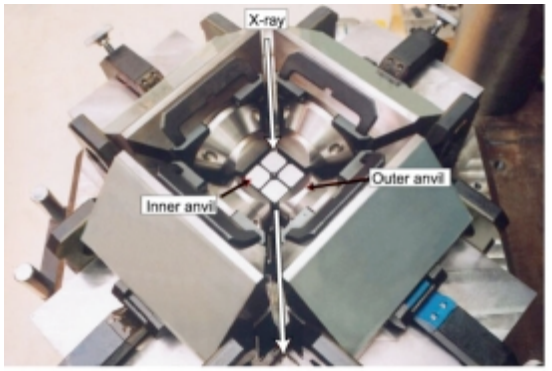

Octahedral cell

Cylindrical guide block/unachored wedges

Walker 6-8 module

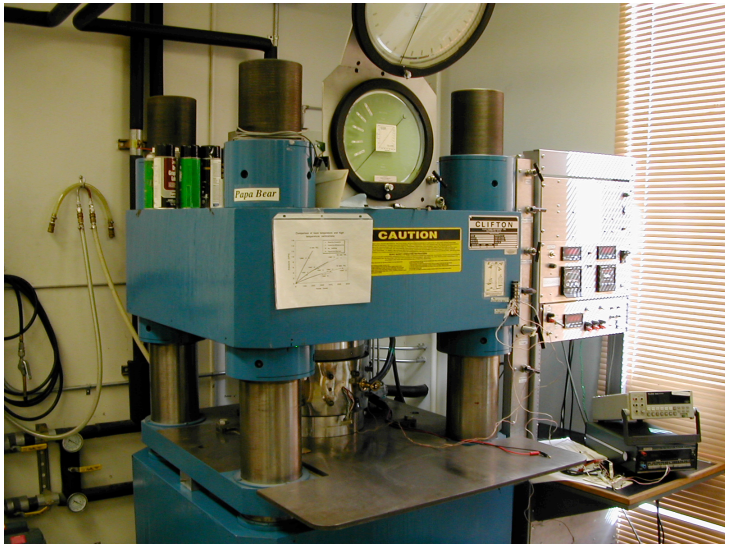

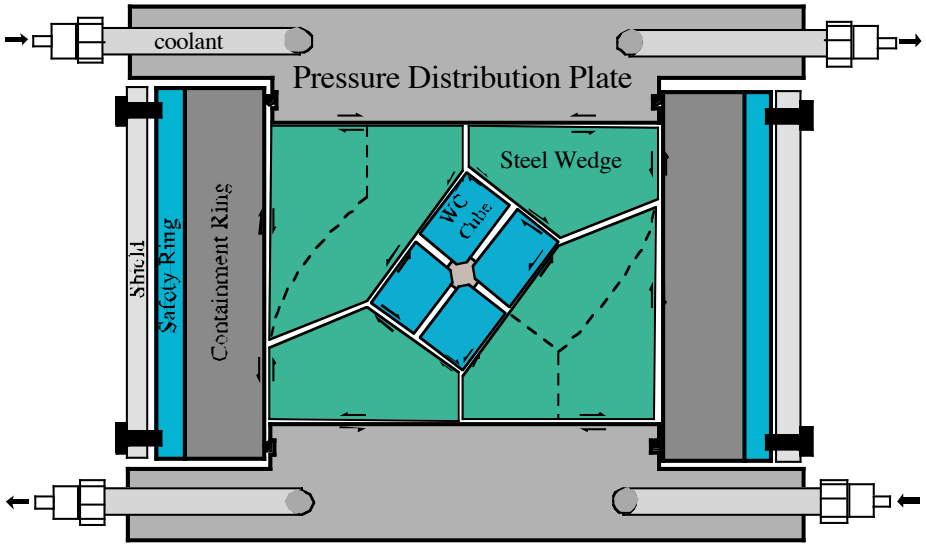

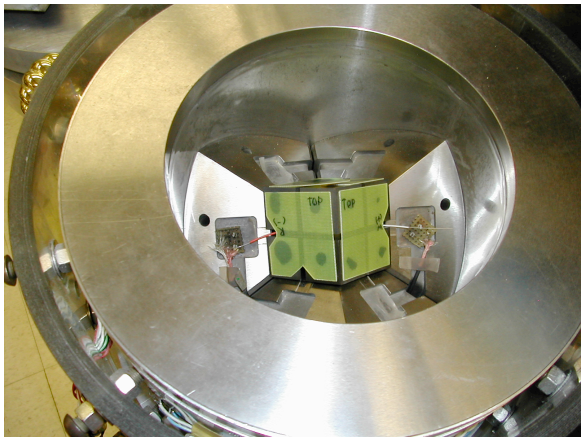

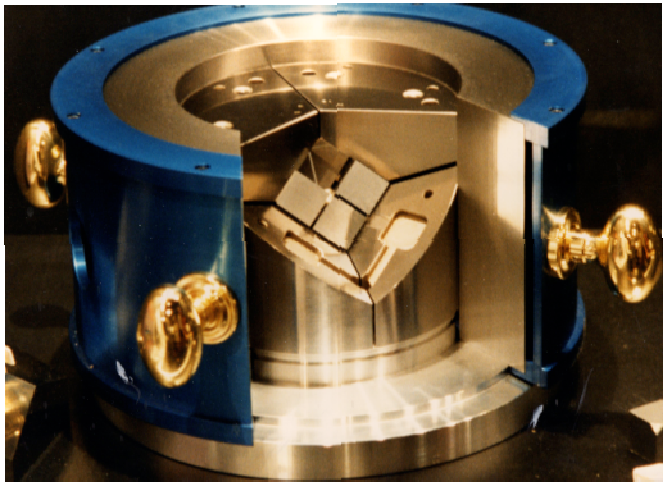

Getting 8-6 (cubic) module

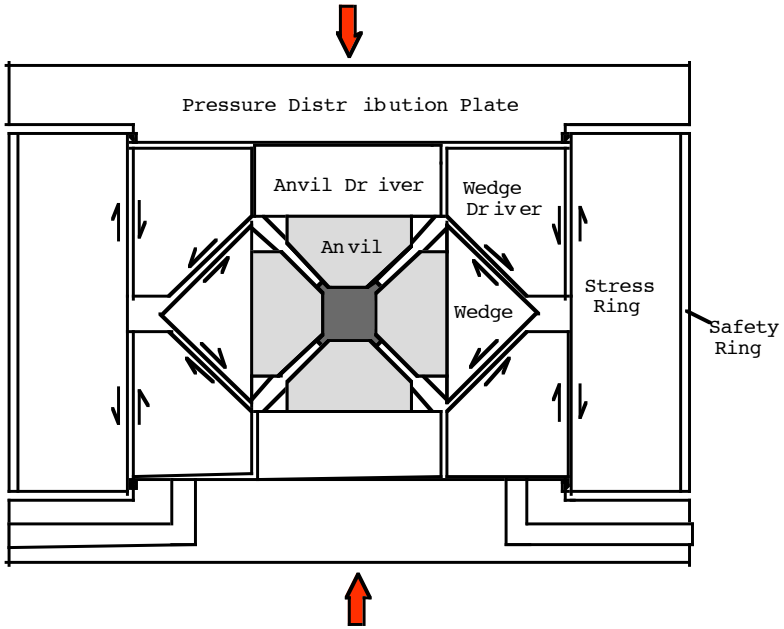

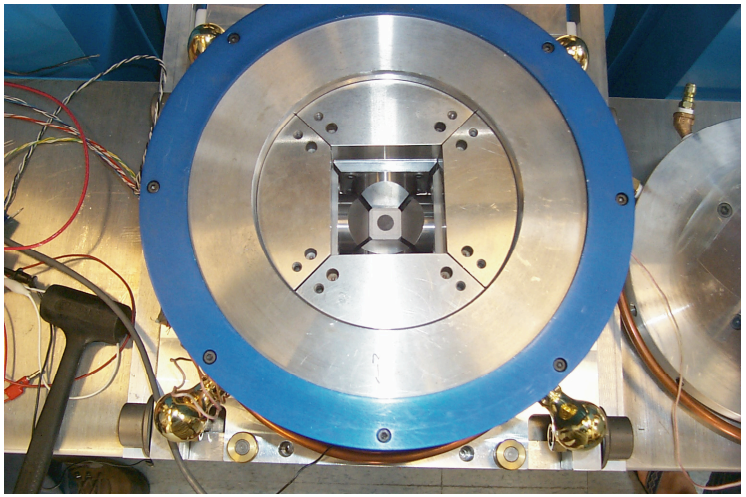

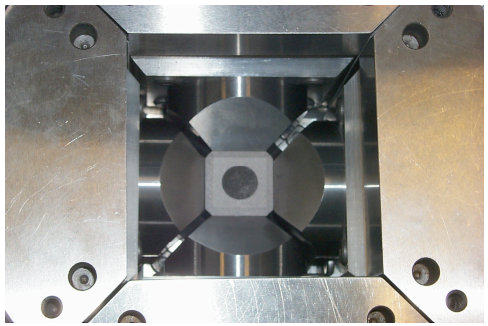

24/19 assembly

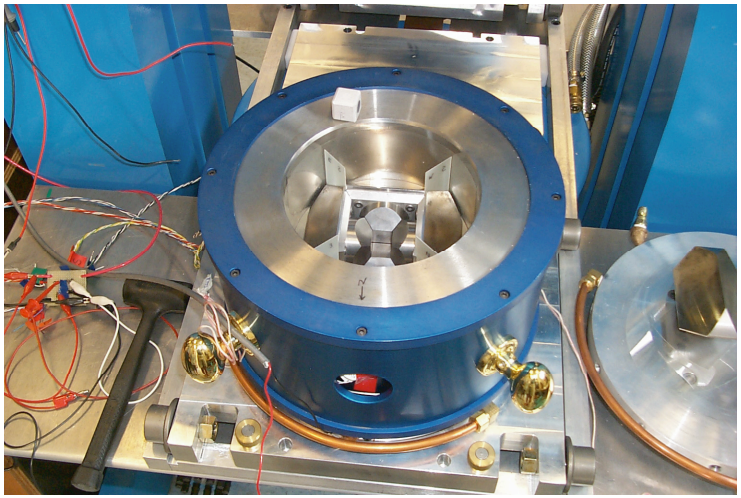

Split-cylinder 6-8 systems

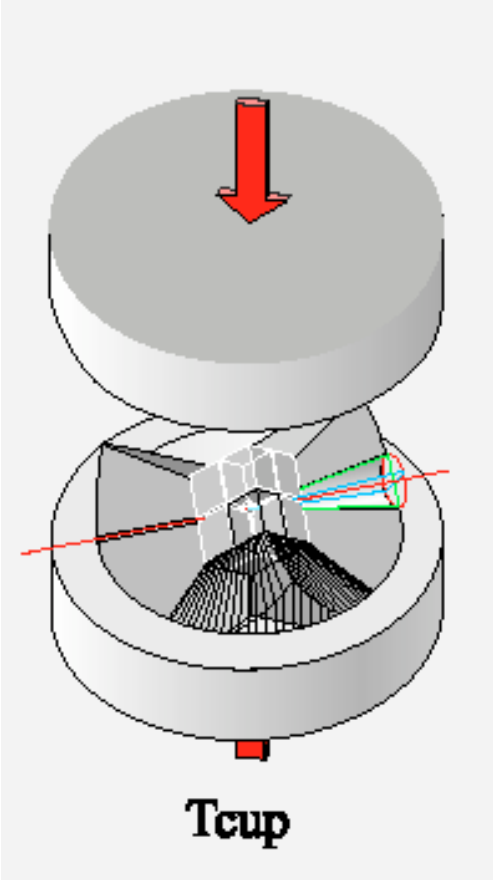

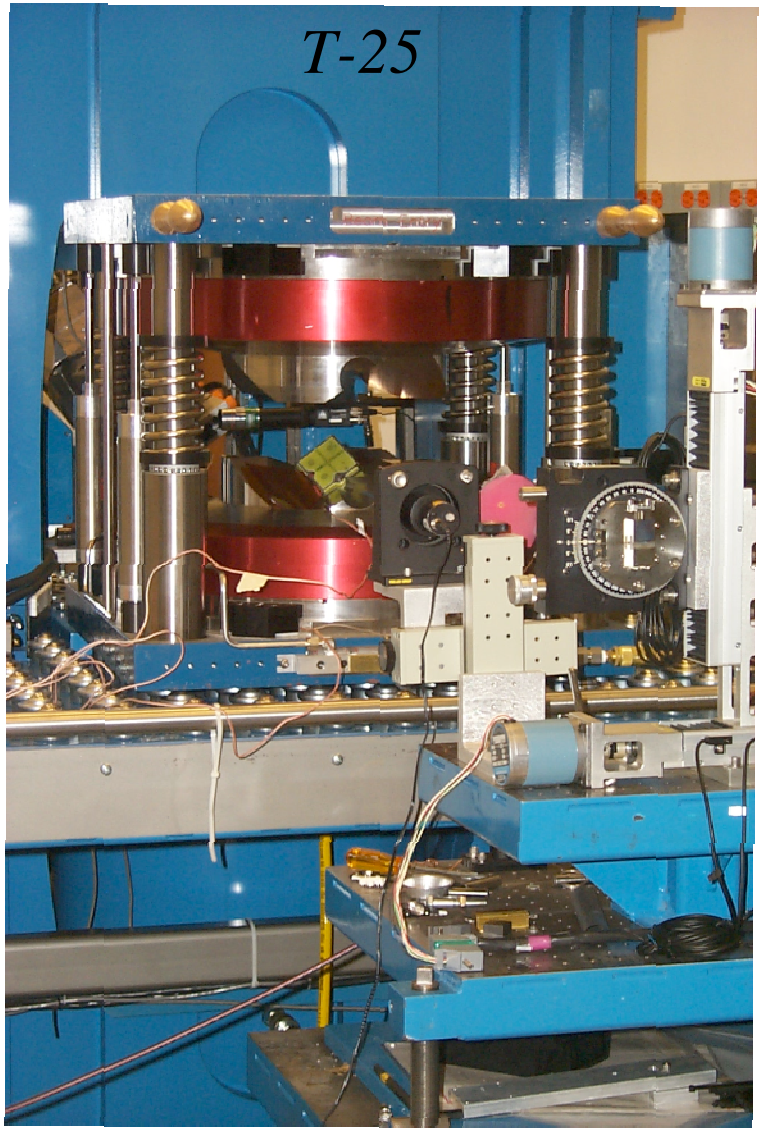

Bayreuth Large Volume Multianvil Apparatus

Split-cylinder

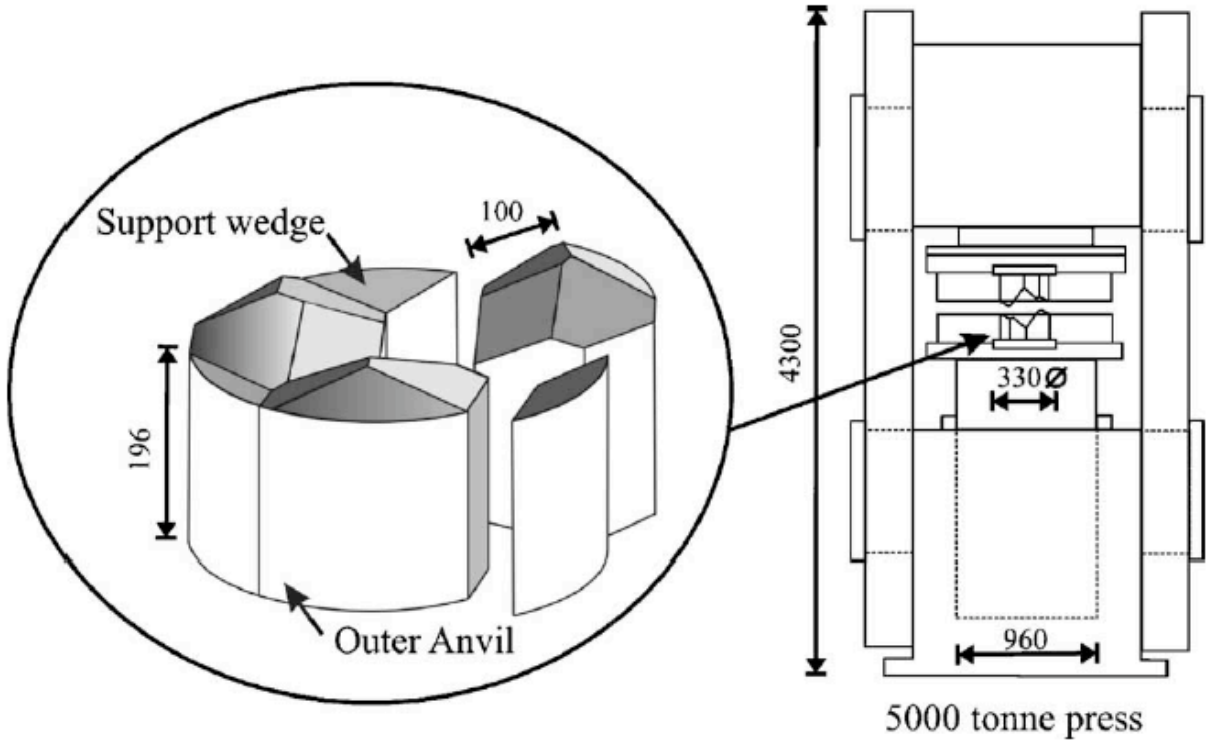

Fig. 1. Schematic diagram of the six wedges of the guide block. The three outer-anvils are separated along the outer circumference by three support wedges (see text for details). The inset to the right shows the 5000 t (50 MN) press frame with the two guide blocks inside steel platens on top of the 960 mm diameter ram. All dimensions are in millimetre.

D.J. Frost et al. (2004, Physics of the Earth and Planetary Interiors 143–144, 507–514

Walker 6/8 module

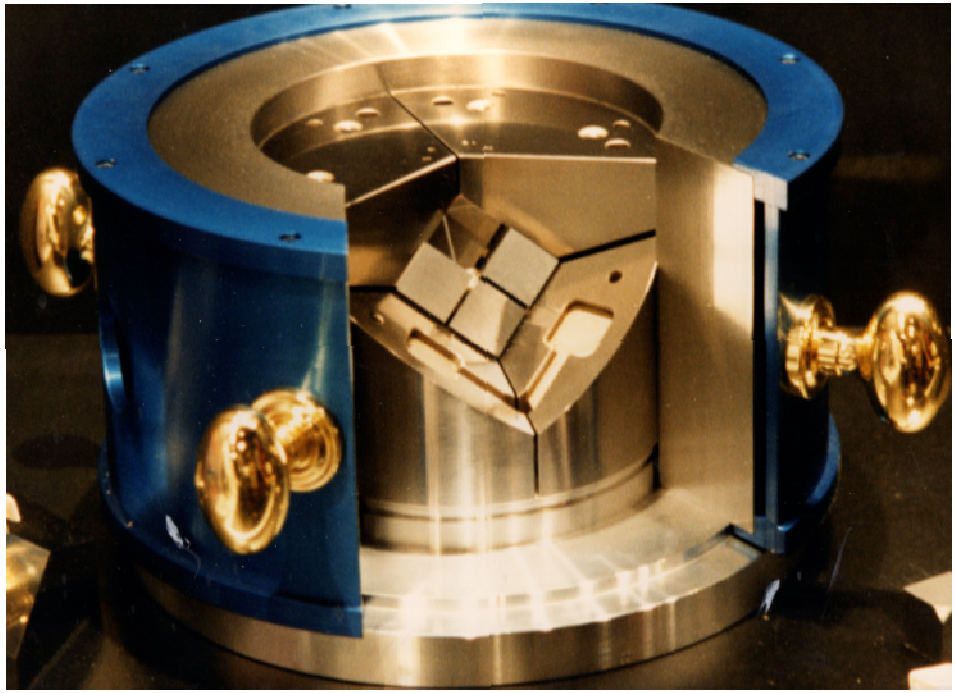

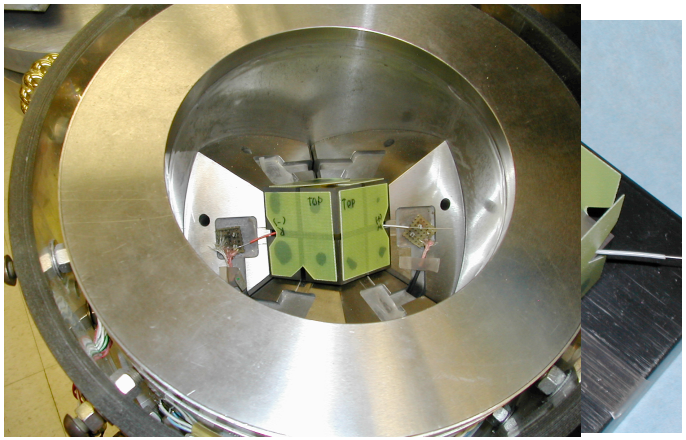

Materials:

Pressure distribution plates: aircraft-quality aluminum base, hardened stainless steel (RC44-46) contact plate

Stress/containment ring: M2 tool steel, upset forging (RC38-40)

Safety ring: ductile SS w/ aluminum shield

Wedges: M2 tool steel (RC44-46)

Anvils: submicron-grade, sintered-HIP, tungsten carbide; cubic BN; diamond

Glide surfaces: PTFE coated mylar; epoxy-filled fiberglass (G10) pads

Loading and Friction

Walker 6-8 module

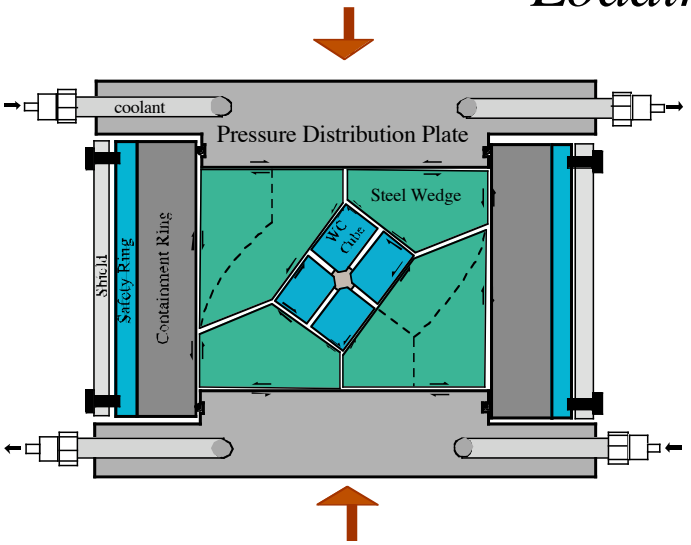

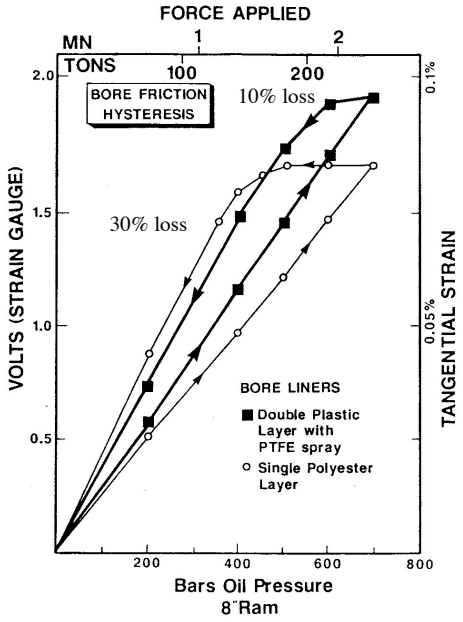

Fig. 3. Strain vs. load on press. Linear loading curves show markedly nonlinear unloading. Bore friction on the wedges is reduced through the expedient of providing a lubricated slip surface of plastic on plastic. Walker et al., 1990

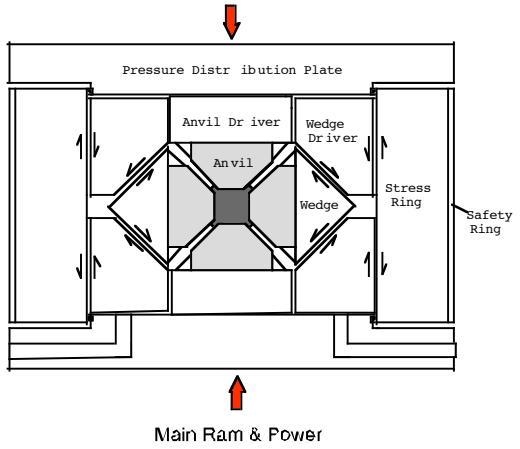

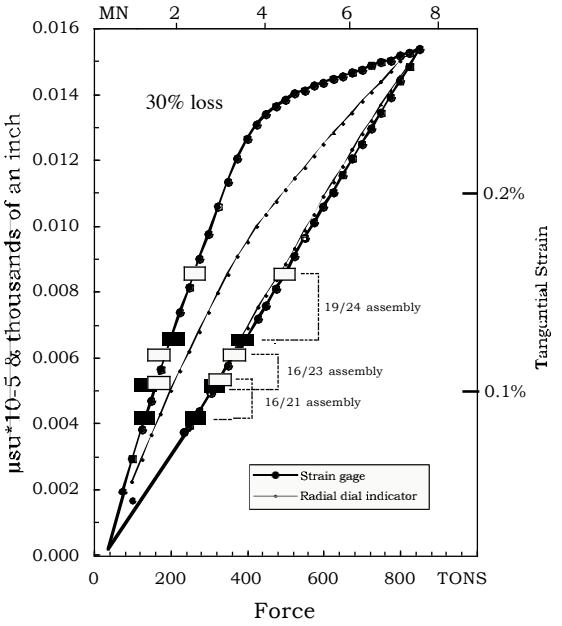

Swelling of the stress ring with the cubic anvil wedge nest and assembly under the uniaxial load from the press. The wedge driver-stress ring interface is lubicated by two sheets of mylar coated with PTFE spray. The heavy line is the strain (in micro-strain units) as measured by strain gauges. The light solid line shows the radial swelling of the stress ring (in thousands of an inch) as measured by dial indicator. The diameter of the stress rIng increased by 0.030" (0.28% strain) on loading of the wedge nest to 850 tons and is fully recoverable on decompression. Non-linear unloading reflects binding of the wedges by ring. Extent of hysteresis suggest > 30% of the thrust lost to friction along the contacting surfaces of the bore and wedge drivers and wedge drivers and wedges. The hysteresis for Bi metal transitions shown by (filled rectangles - Bi I-II; unfilled rectangles - Bi II-III') for various assemblies agrees well with the stress-strain loop determined for the stress ring. (Lesher et al., 2000)

Getting 8-6 module

6-8 Tcup

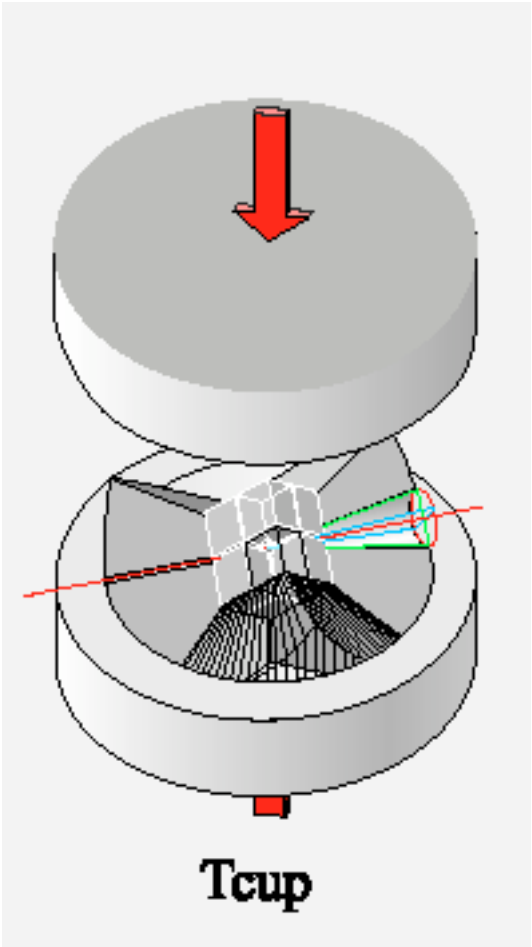

6-8 Tcup

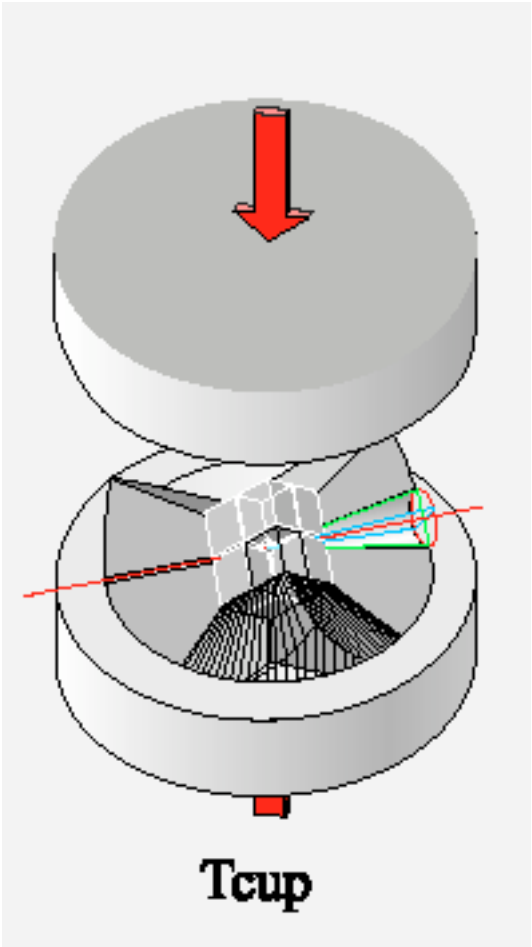

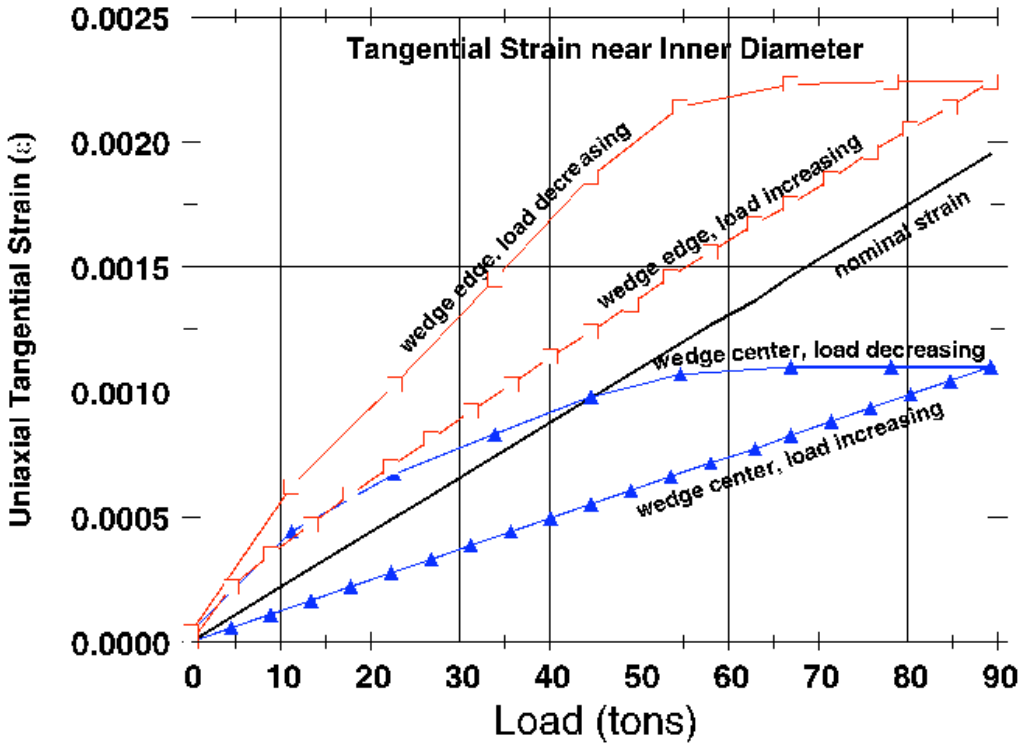

Strain in containment ring near the inner diameter. Maximum strain is found at the boundary between two of the first-stage anvils (wedge edges).

(Vaughan et al.)

Carbide is the weakest link!

Getting et al., 1993

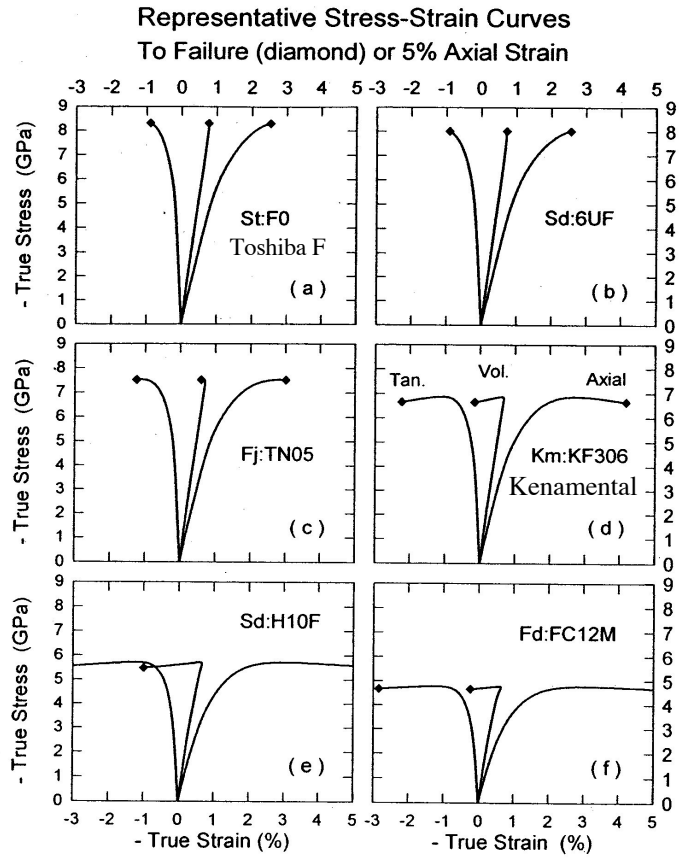

Figure 2
Representative compressive stress-strain curves for six grades. Axial, tangential, and volumetric curves are shown for each grade as identified in (d). The two strongest grades, (a) and (b), failed before reaching their ultimate potential stress as demonstrated by the positive slope of the axial stress-strain curve at failure. The other four grades achieved their maximum potential stress and all exhibit some degree of dilatancy as evidenced by the abrupt corner in their volumetric stress-strain curves and the subsequent increase in volume. Grades are designated on the plots. Manufacturer abbreviations are as follows: St: Sumitomo, Sd: Sandvik, Fj: Fujilloy, Km: Kennametal, Fd: Federal Carbide.

Submicron Grade Carbides
(Data from Getting et al., 1993, PAGEOPH, v. 141, 545-577)

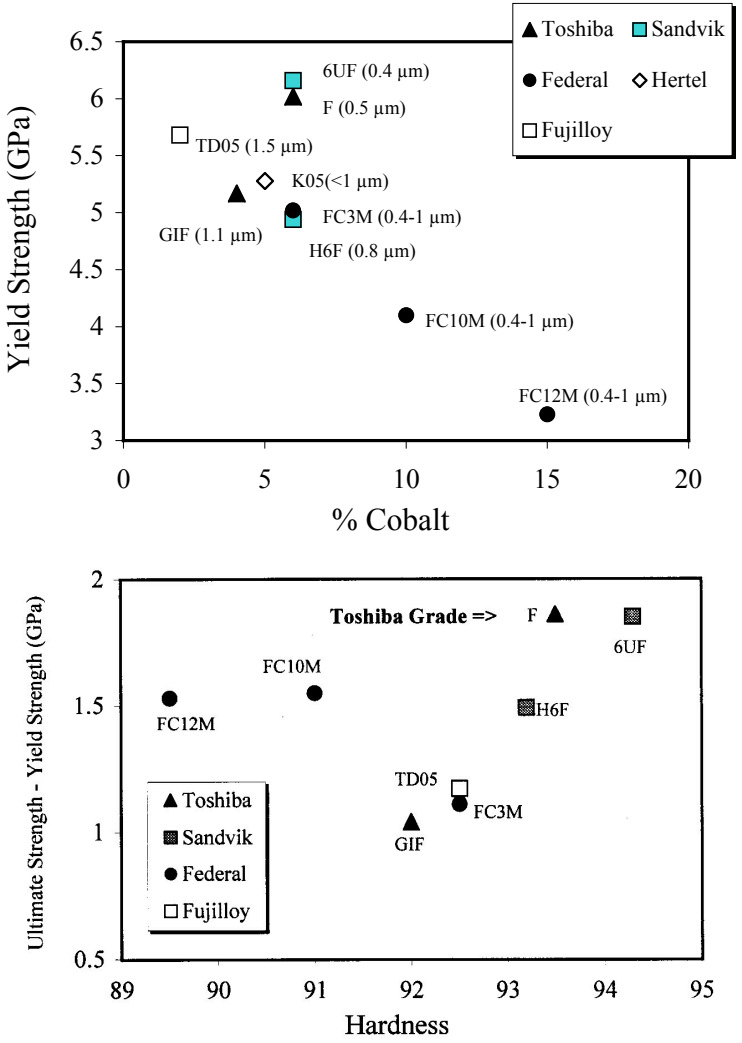

Look for carbide that is tough and hard - Toshiba F grade

Liebermann & Wang (1992)

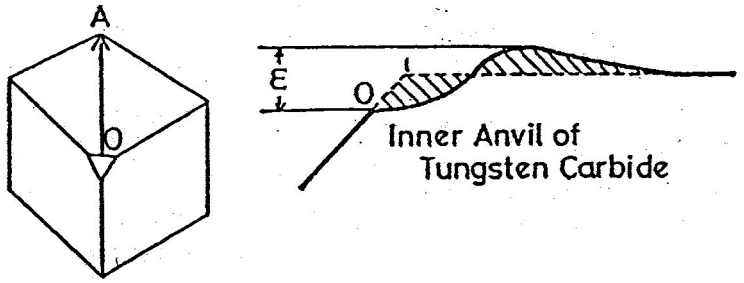

Figure 6. Typical plastic deformation observed in the tungsten carbide cubes. For the 7/2 assembly and Type C gaskets (Fig. 7, the amplitude ε of the deformation after achieving the GaAs transition has been measured for the Kennametal KZ 313 (150 micron), Hertel KF1 HIP (100 micron) and Toshiba F (75 micron) grades.

Gwanmesia et al. (1993)

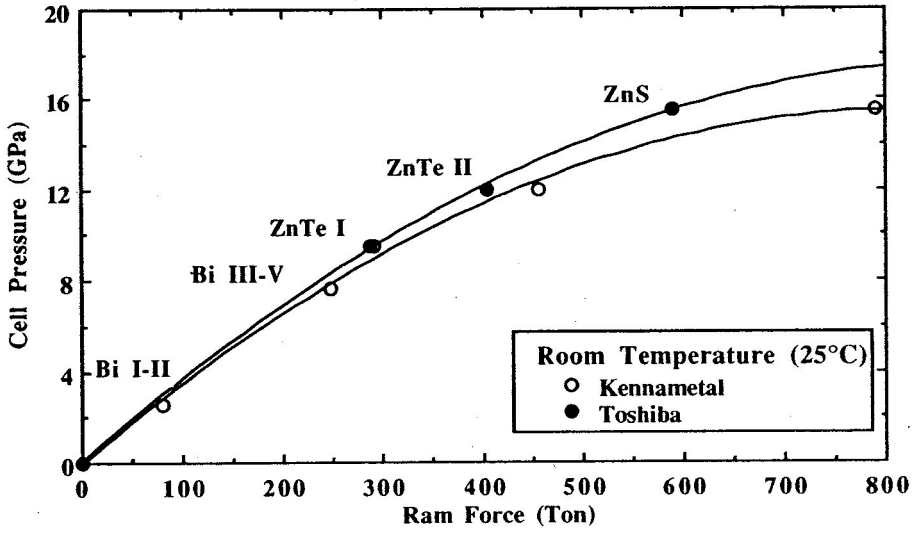

Figure 6

Pressure calibration of 14/7/5 cell assemblies at room temperature using both Kennametal (open circles) and Toshiba (closed circles) tungsten carbide cubes.

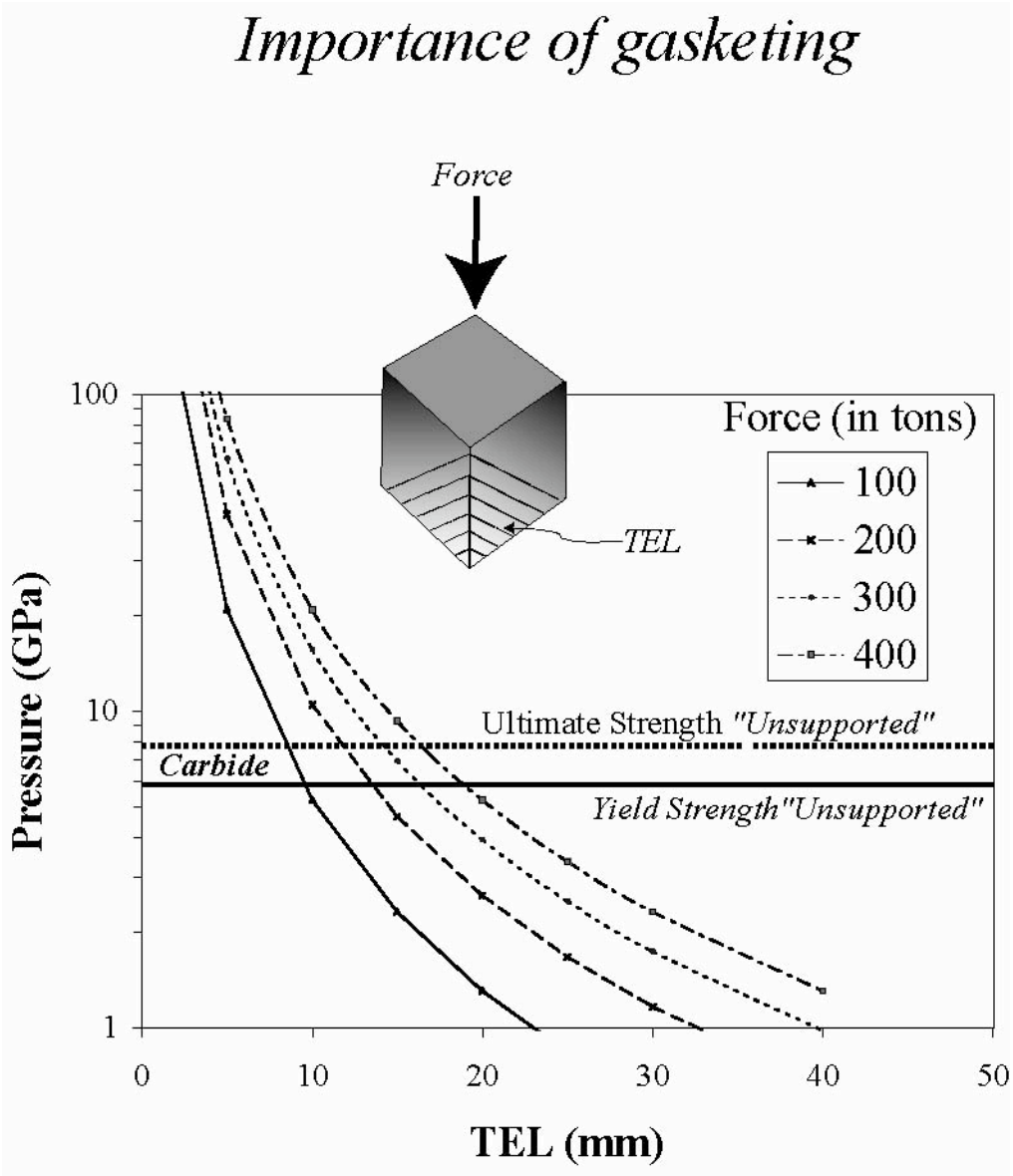
Importance of gasketing
Force
TEL
Force (in tons)
100
200
300
400
Ultimate Strength "Unsupported"
Carbide
Yield Strength"Unsupported"
Pressure (GPa)
100
10
1
0
10
20
30
40
50
TEL (mm)

Importance of gasketing

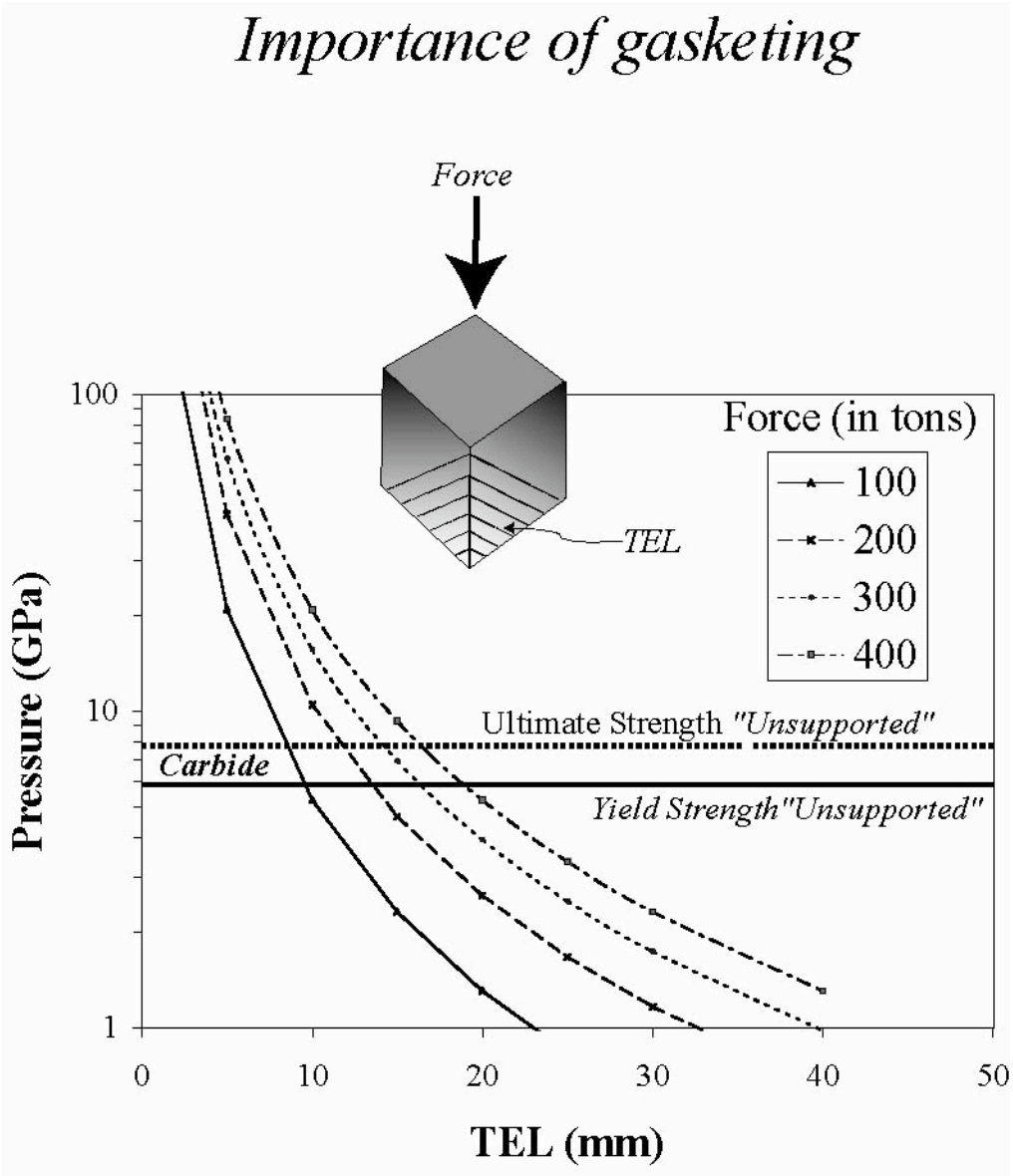

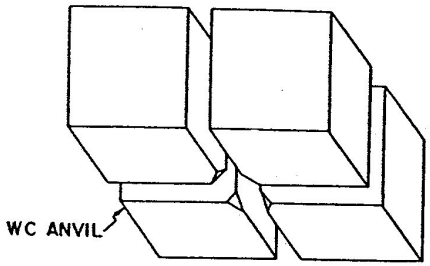

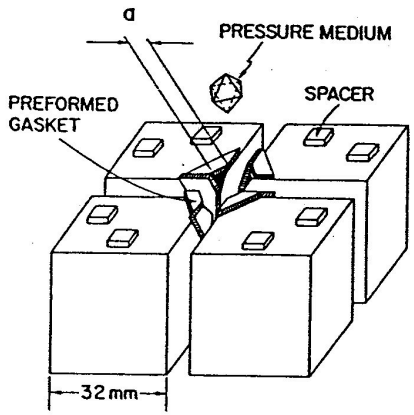

Cell Assemblies

Octahedron

pyrophyllite

semi-sintered MgO ($^{+}Cr_2O_3$; machined or casted)

Gaskets

pyrophyllite (preformed)

semi-sintered MgO (cast w/ octahedron)

-back-up Teflon tape-

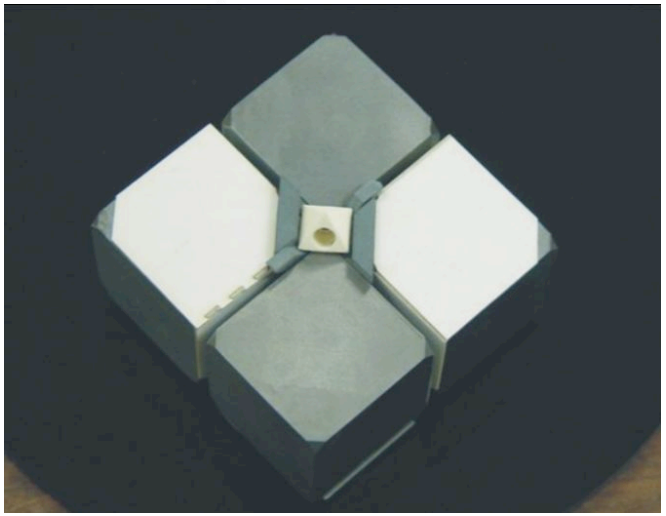

COMPRES assembly
(K Leineweber)

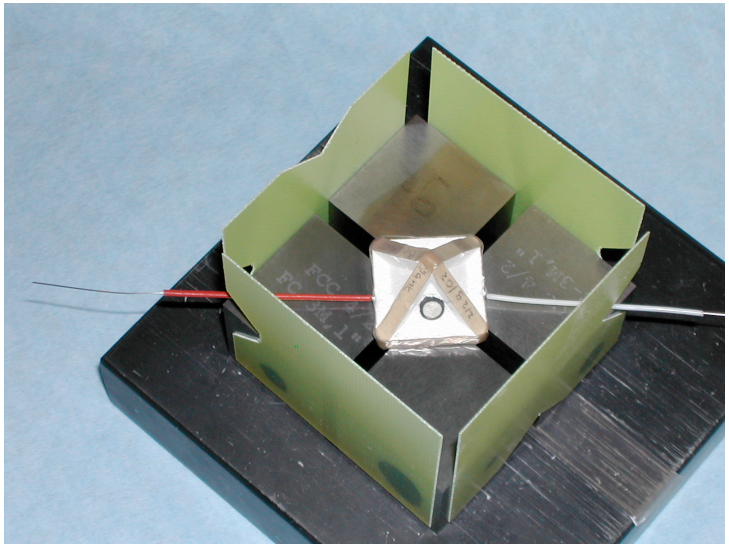

Material: Aremco 584 (MgO)
Porosity: 40% (fired)

http://www2.bnl.gov/sam85/tcup/html/tcup.html (Vaughan et al.)

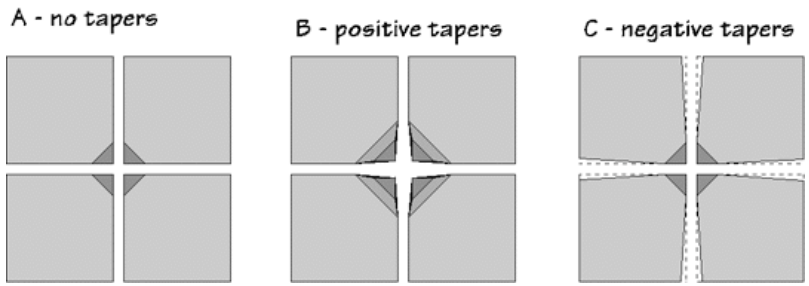

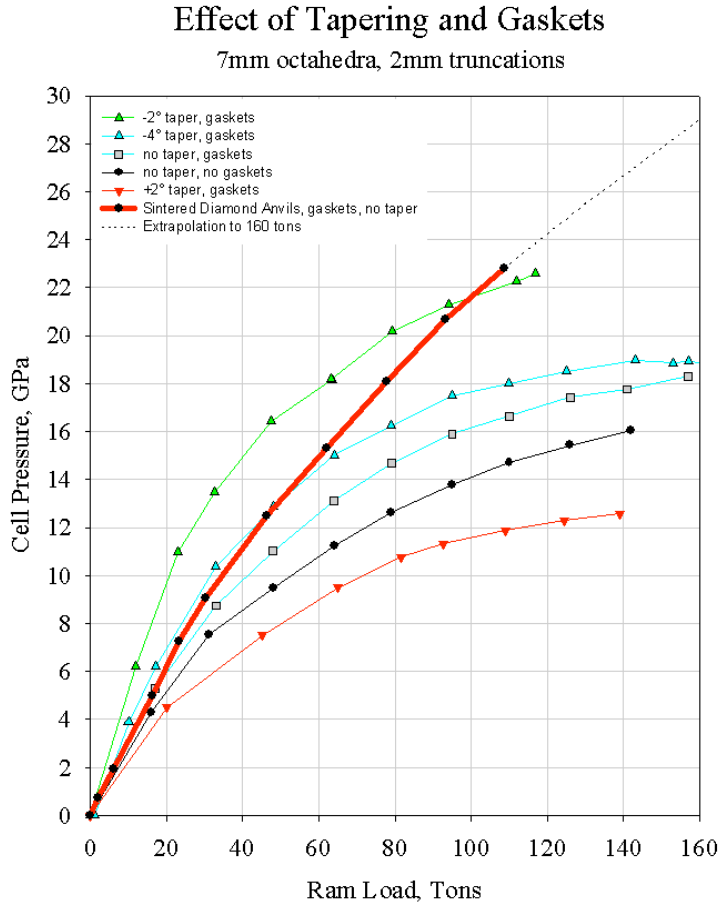

The Pressure Cell

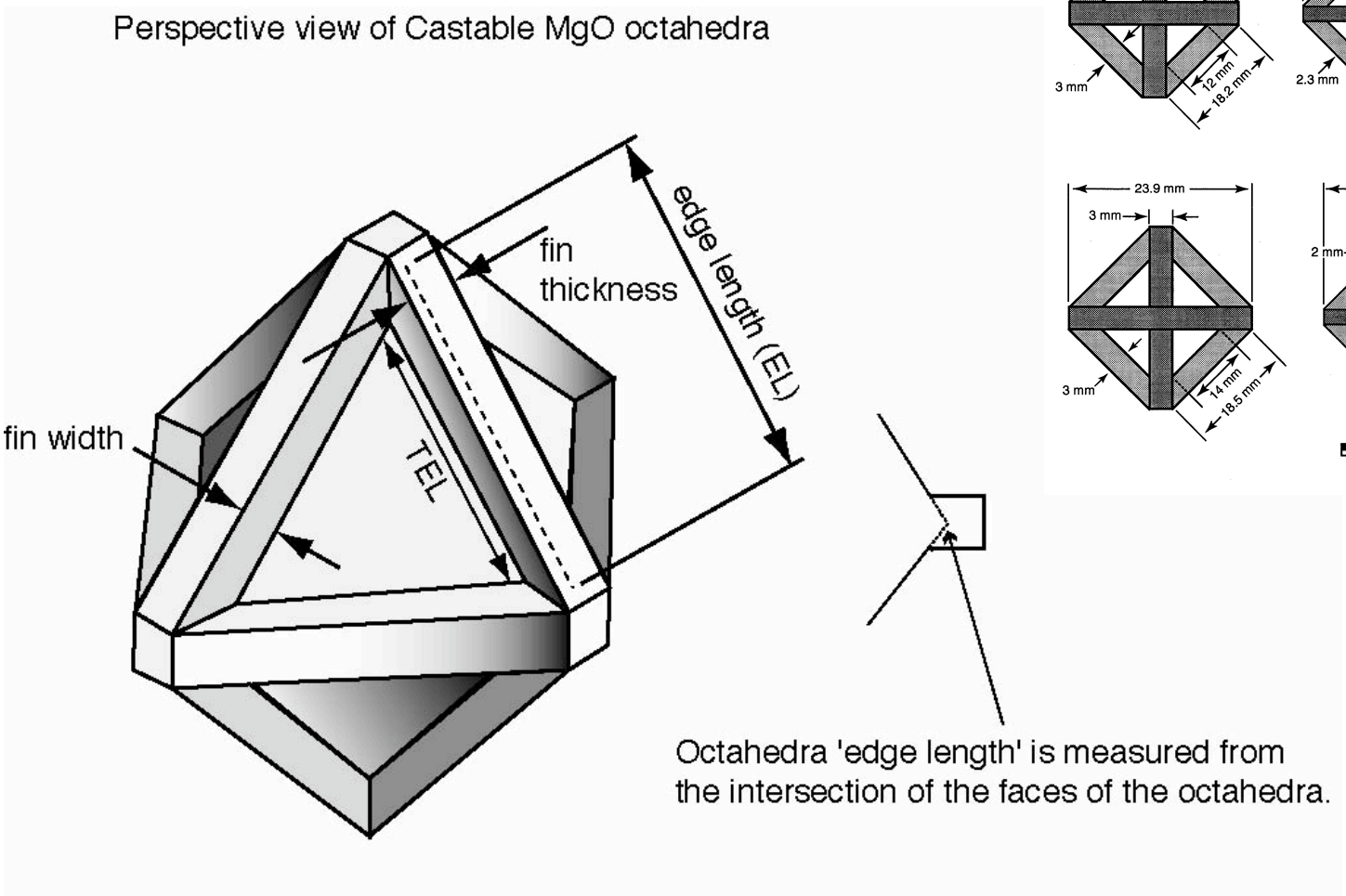

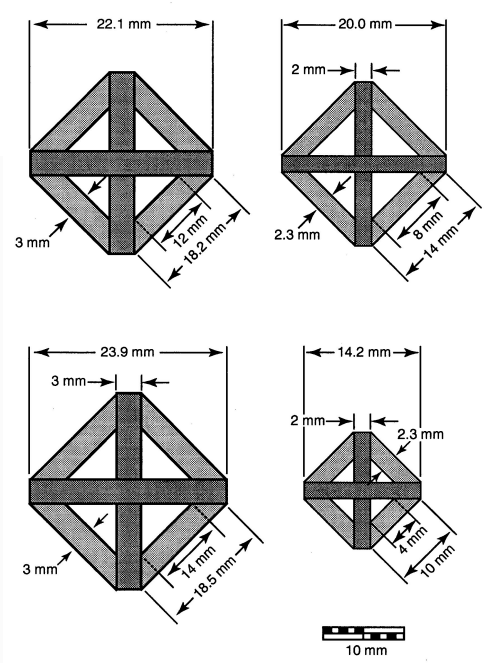

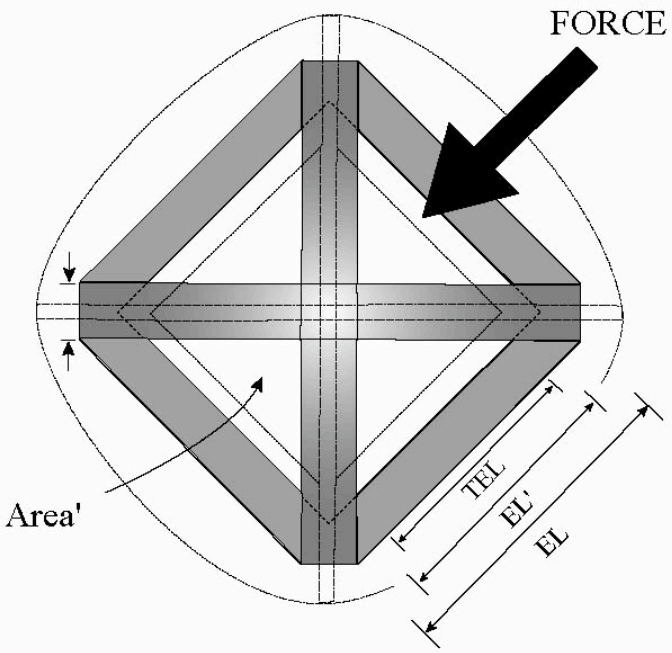

$$V_{original} = \sqrt{2}/3\ (EL)^3$$

Porosity correction*: $V_{densified} = V_{original}\ (1 - \phi_{fired}) = \sqrt{2}/3\ (EL')^3$

$$P = 0.25\ Force/Area' = 0.5\ Force/(EL' \bullet height)$$

Compressible medium: $P \sim \Delta V/V_o\ K$

*Aremco 584 (MgO): 40% porosity (fired)

Incompressible vs. compressible

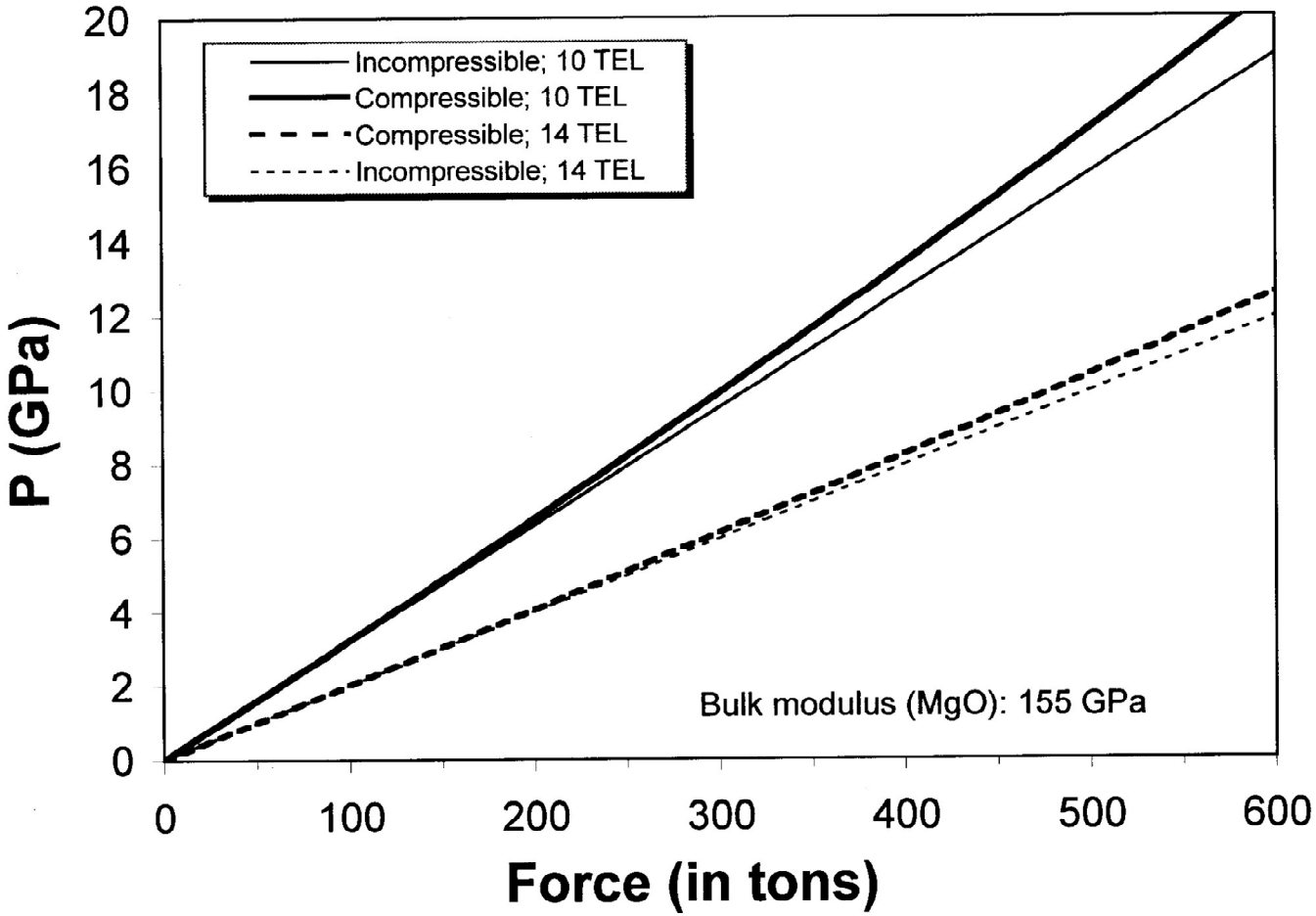

Porosity

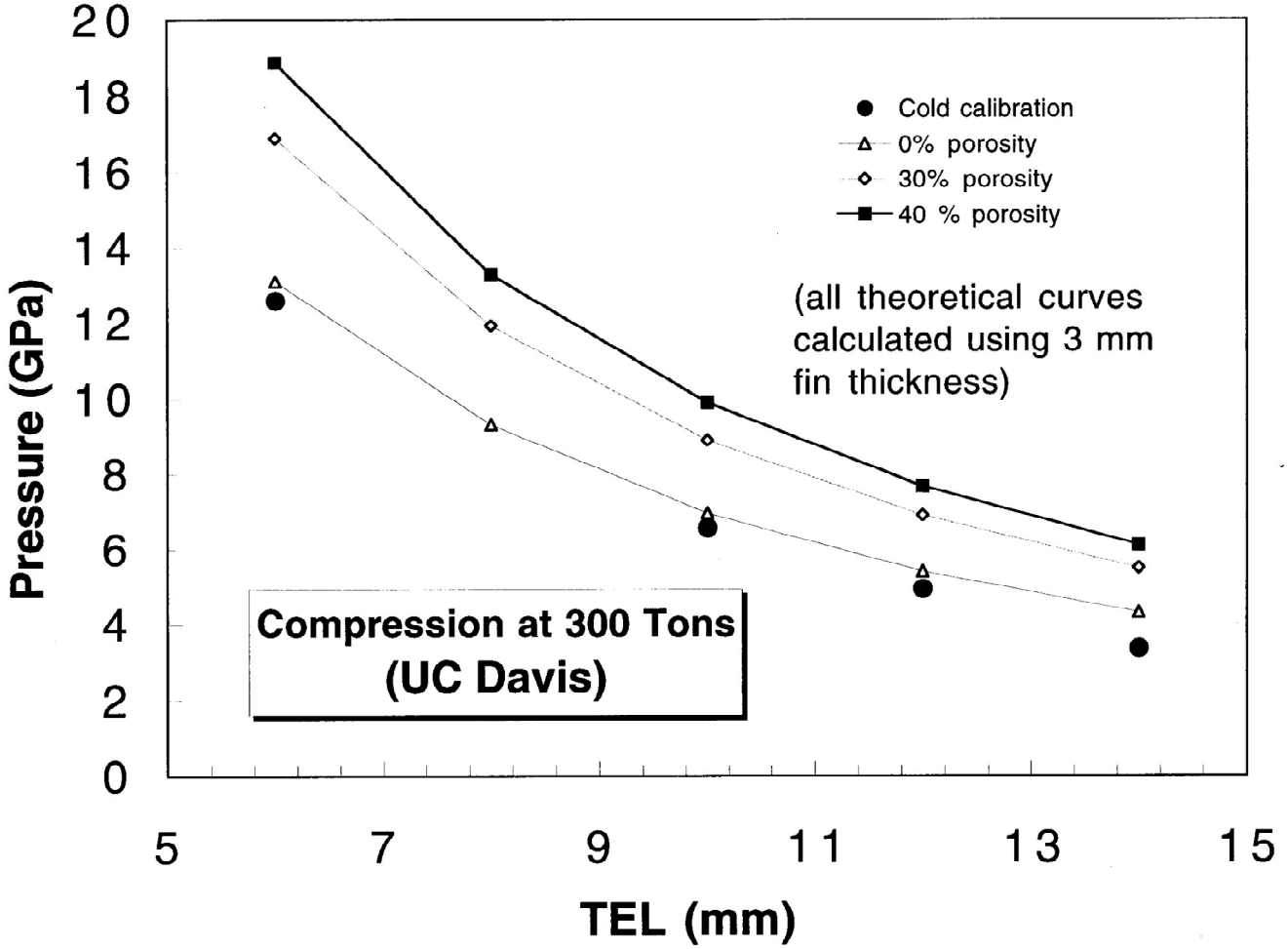
Pressure (GPa)
20
18
16
14
12
10
8
6
4
2
0
5
7
9
11
13
15
TEL (mm)
Cold calibration
0% porosity
30% porosity
40 % porosity
(all theoretical curves calculated using 3 mm fin thickness)
Compression at 300 Tons
(UC Davis)

Carbide support vs. Efficiency

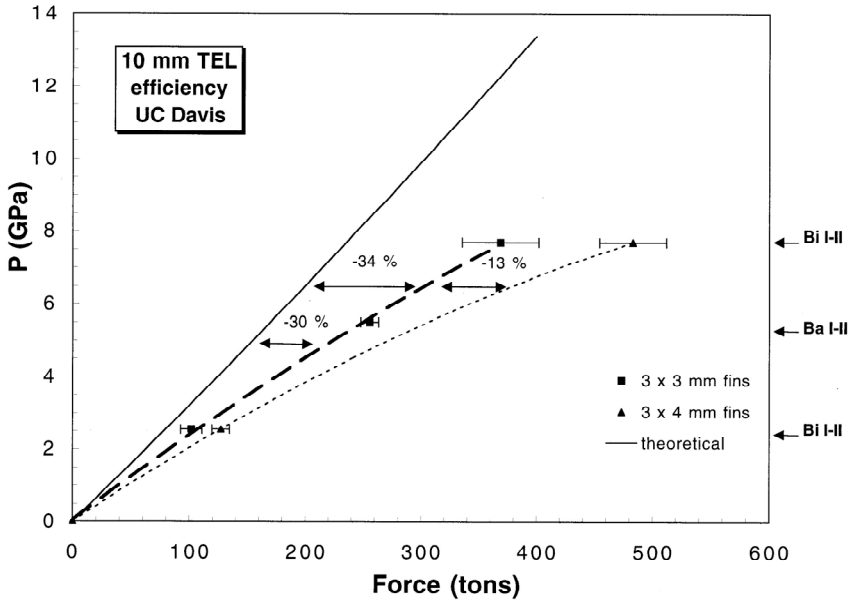

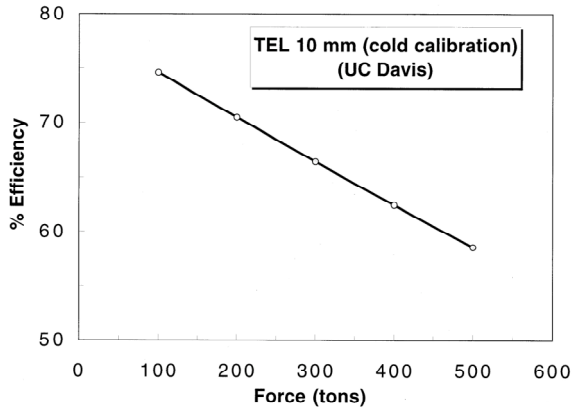

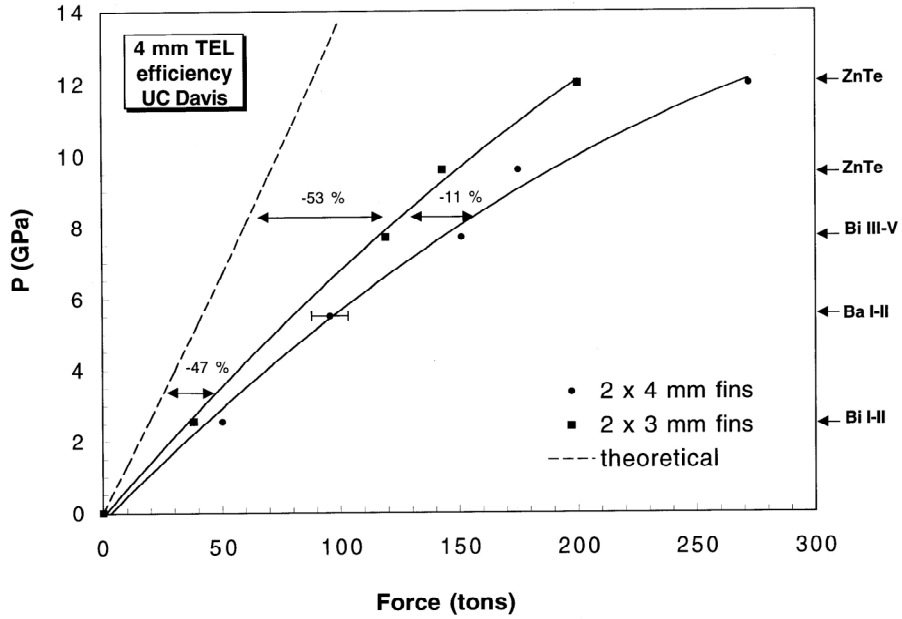

Heat Generation

Furnace Types

Graphite

- straight-wall or stepped
- resistor; 20:1 stepdown
- < diamond stability

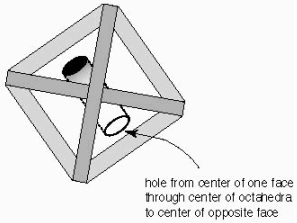

$LaCrO_3$

- straight-wall or stepped
- semiconductor at h-T; <10:1 stepdown

Re foil, Inconel

18/11 Assembly

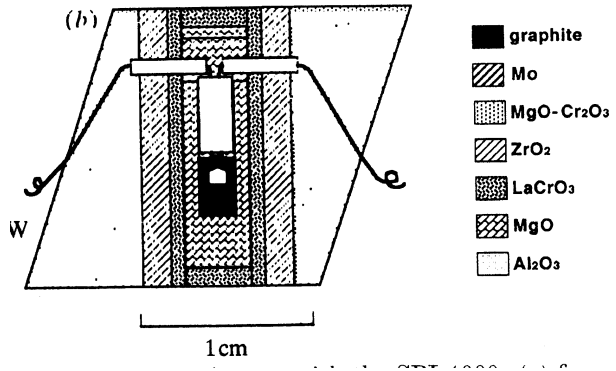

14/8 Assembly

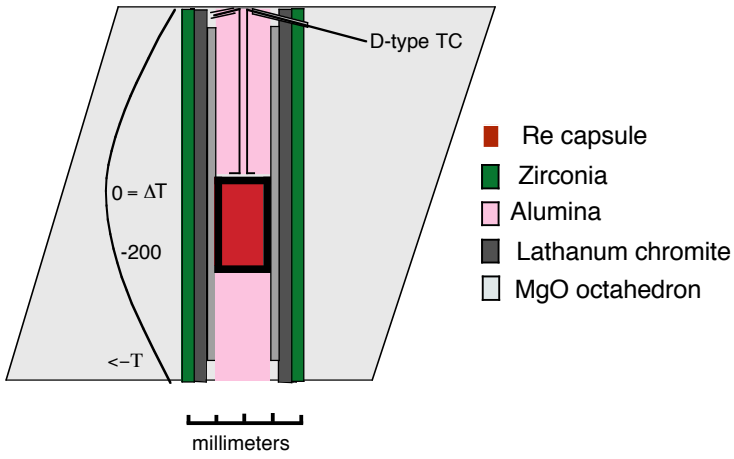

Re capsule
Zirconia
Alumina
Lathanum chromite
MgO octahedron

18/11 Assembly

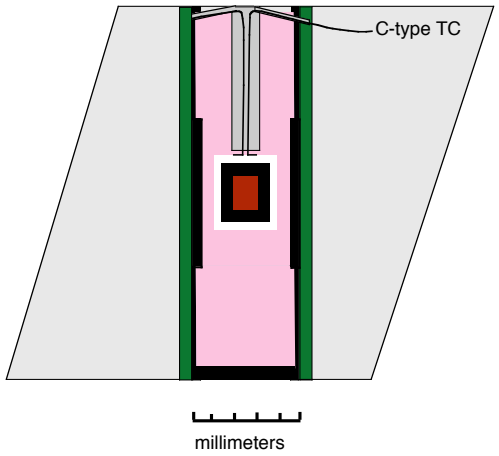

Pt
Graphite
MgO & Alumina — Filler rod
TC ceramic sheath
Cast & pre-cast MgO octahedron

Power Consumption

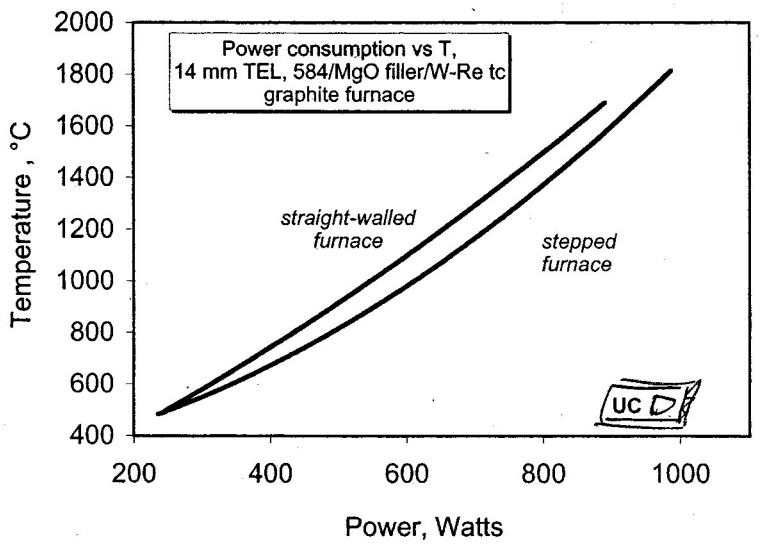

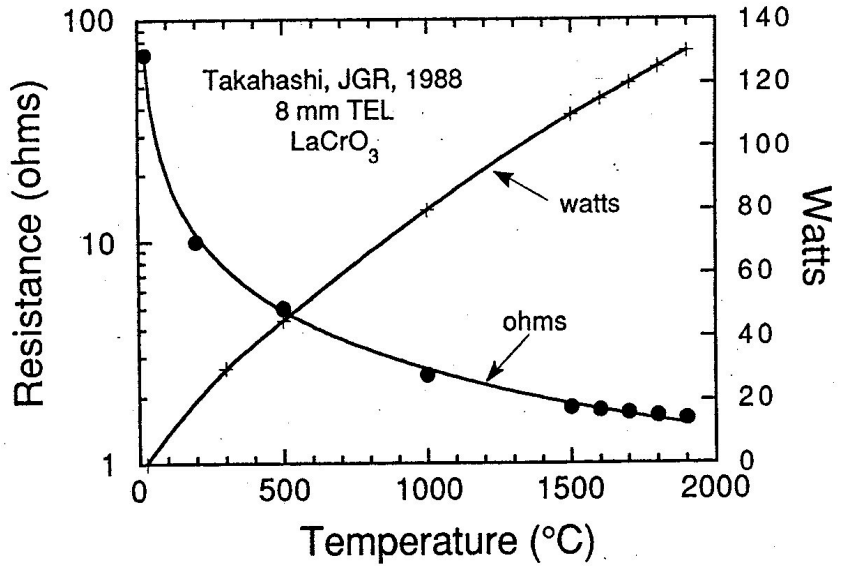

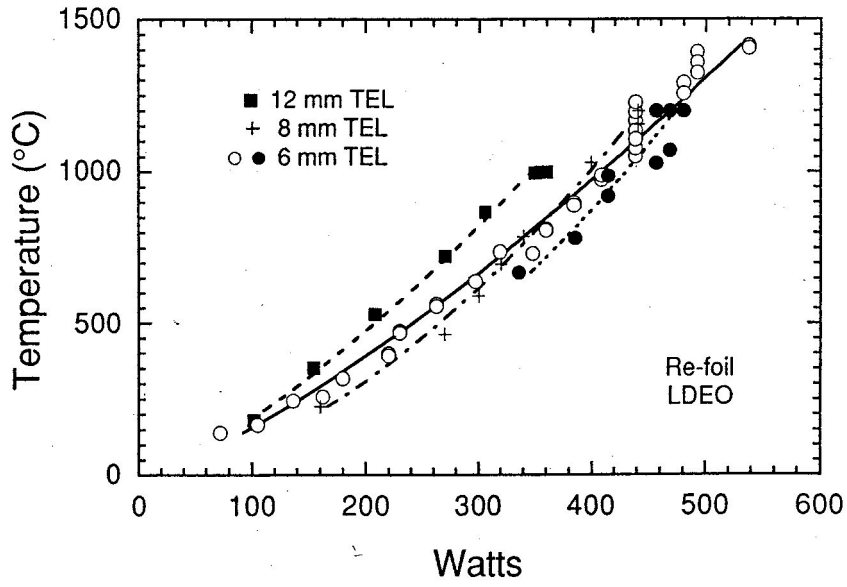

Temperature Control

Thermocouple Configurations

Radial

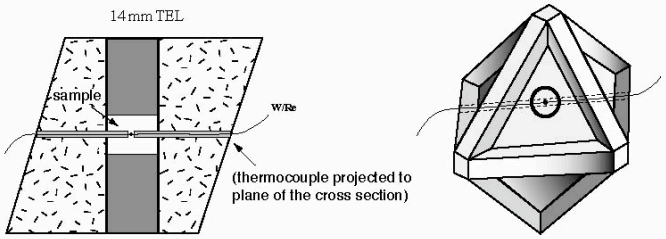

Figure 1. Cross-section and perspective view of assembly with thermocouple wire passed directly through sample in center of assembly.

Axial

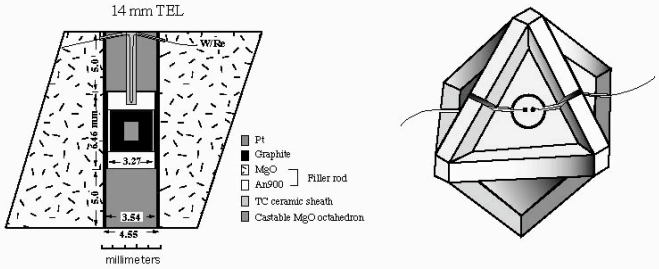

Figure 2. Cross-section and perspective view of assembly with thermocouple wire brought down through top of furnace. Wires are passed through channels cut into octahedra that are filled with alumina cement.

P/T dependence of emf

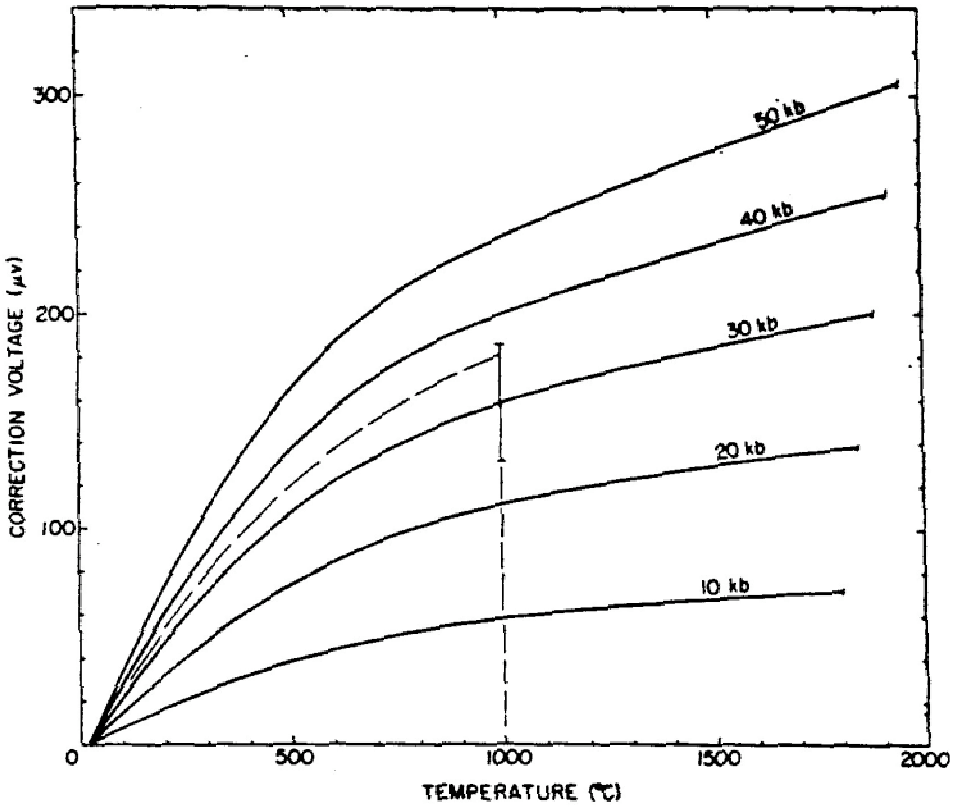

S-type TC

FIG. 11. Corrections for Pt-Pt10Rh thermocouples operating with a seal temperature of 20°C. The dashed lines indicate the upper limits of the experimentally explored region.

Getting & Kennedy (1970)

Poorly characterized for W/Re thermocouples

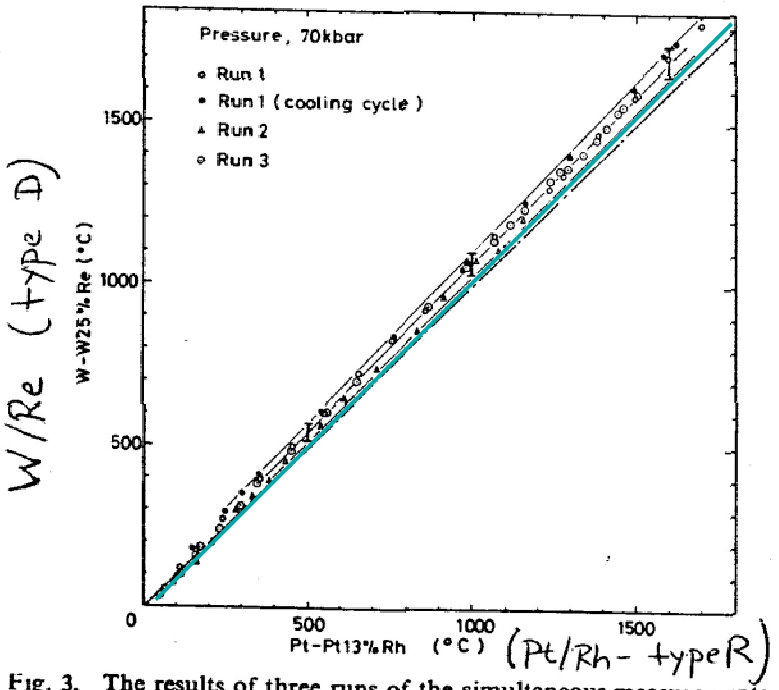

Fig. 3. The results of three runs of the simultaneous measurements of the temperature values indicated by Pt-Pt13%Rh and W-W25%Re thermocouples at 70 kbar. The solid circles are the result of the cooling cycle of Run 1. The others are the results of the heating cycle of three runs.

Ohtani (1979)

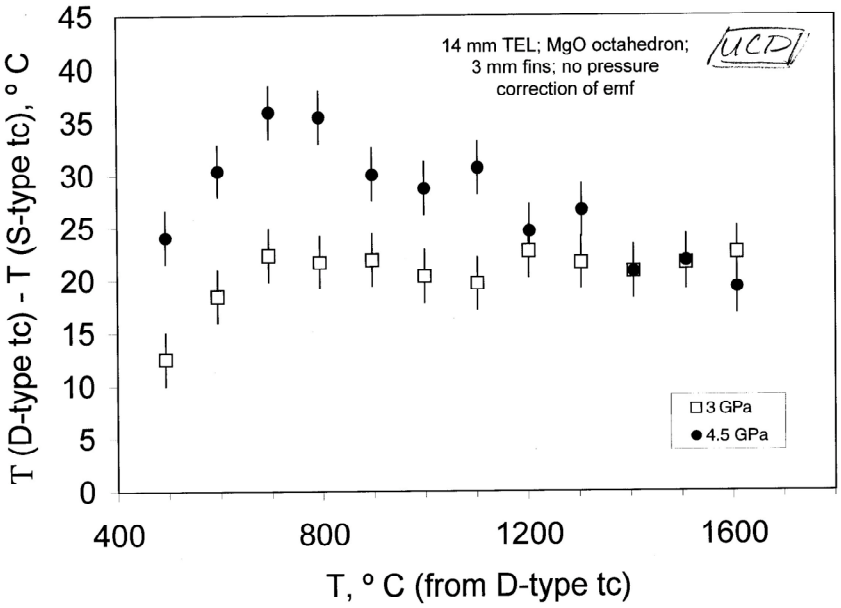

Thermal Gradients

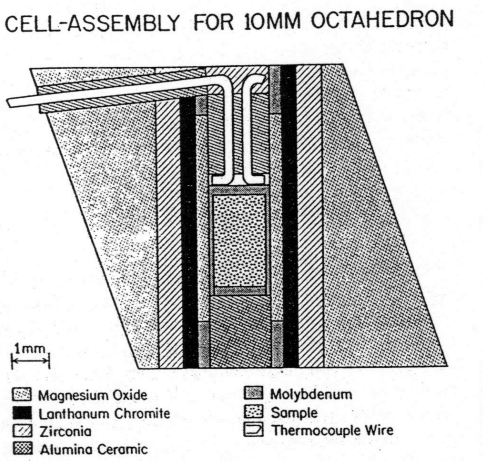

Figure 10. Cell assembly for determining the temperature distribution using the enstatite content of diopsidic pyroxene coexisting with enstatitic pyroxene (from Gasparik, 1989;—rhenium replaces molybdenum as the capsule in the higher temperature experiments of Presnall and Gasparik, 1990).

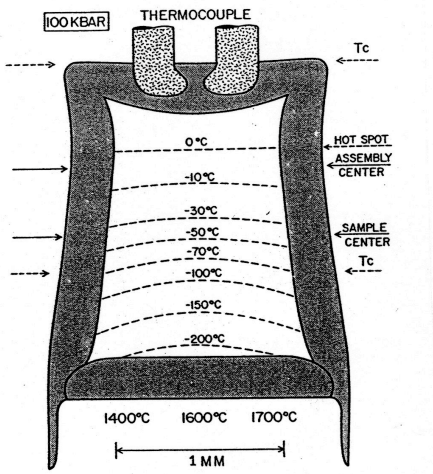

Figure 11. Cross-section of an experimental charge in a 10 mm MgO cell assembly showing the isotherms inferred from the enstatite-diopside data which are in Fig. 3 of Gasparik (1989).

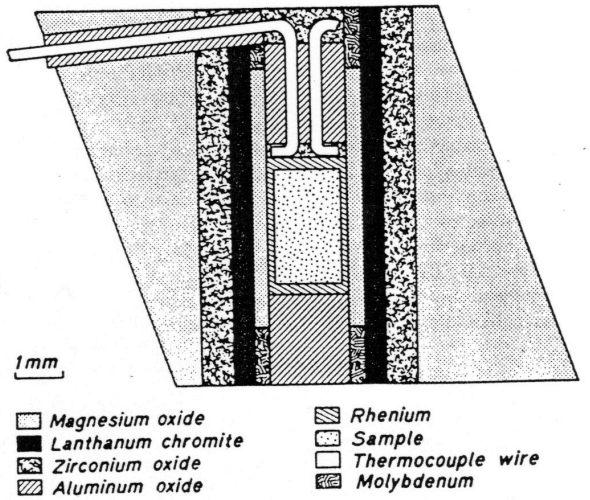

Fig. 1. Assembly of 10-mm octahedron.

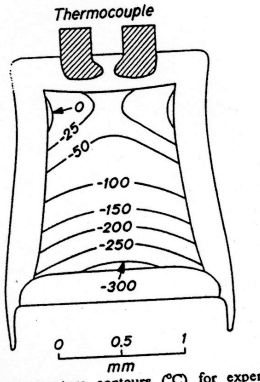

Fig. 2. Relative temperature contours (°C) for experiments in the temperature range 2000°-2150°C. Contours are interpolations based on Figure 3 of *Herzberg et al.* [this issue] with slight modifications of shape based on crystal-liquid isothermal surfaces observed in this study. The pressure cell assembly of *Herzberg et al.* [this issue] is identical to that used here except for their use of Mo capsules. The temperature difference of 300°C between the hot and cold ends of the capsule is consistent with the smaller difference of 200°C reported by *Gasparik* [1989] at lower temperatures (1400°-1700°C).

5 GPa/1950 ºC/8 min

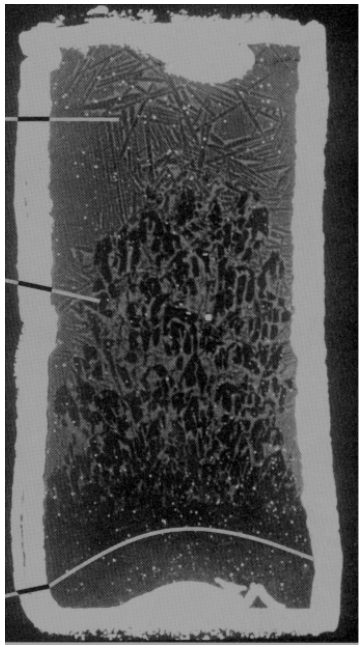

Zhang and Herzberg (1994)

Consequences of large thermal gradients

5 GPa/1700ºC/10 min

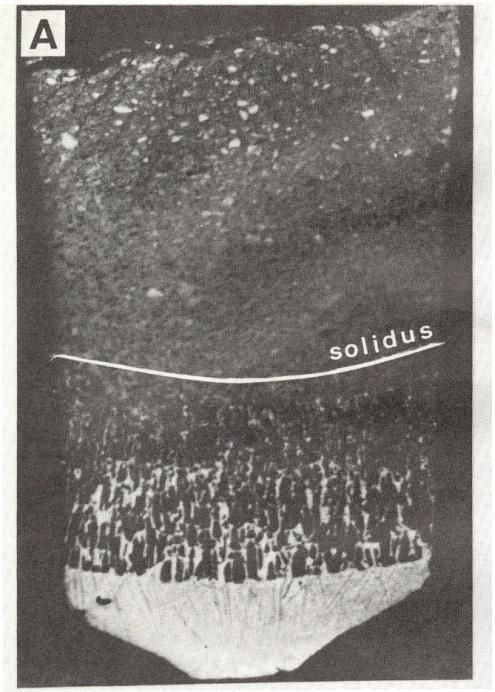

Takahashi (1986)

Thermal Migration

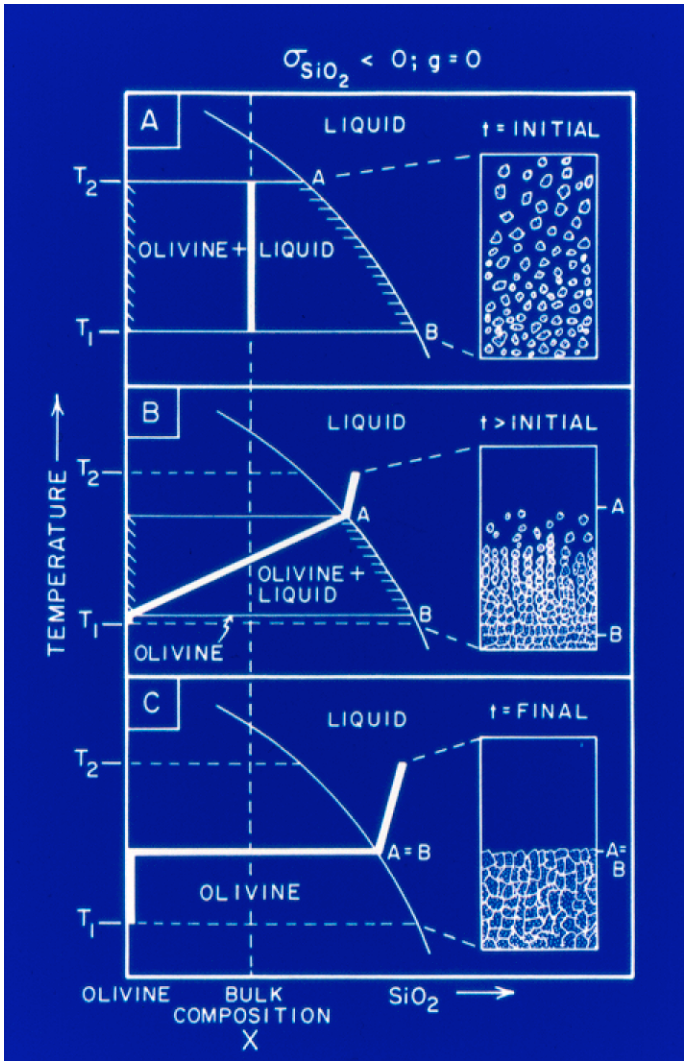

Lesher and Walker (1988)

Minimize thermal gradients

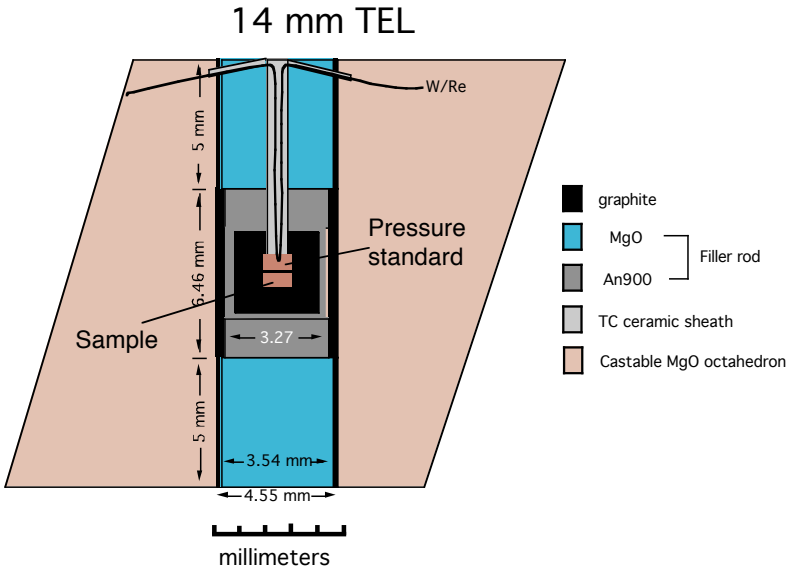

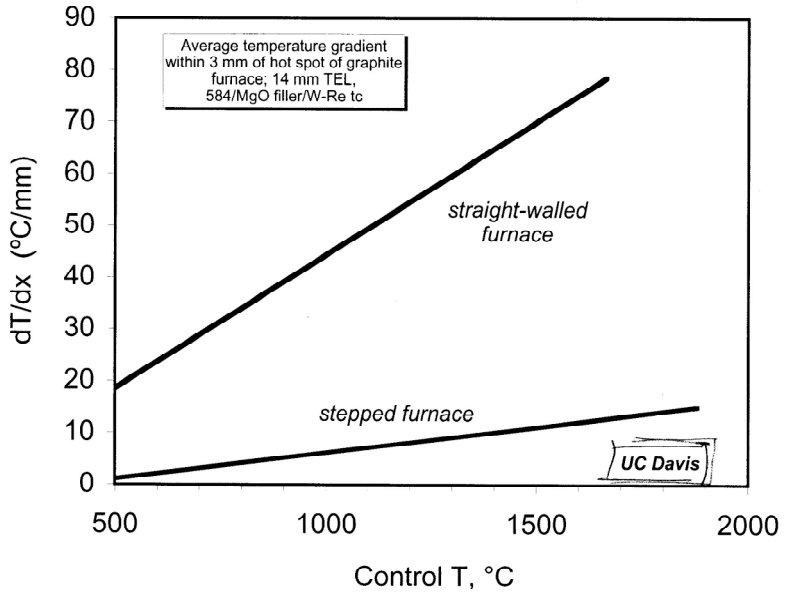

Cross-section of stepped heater assembly.

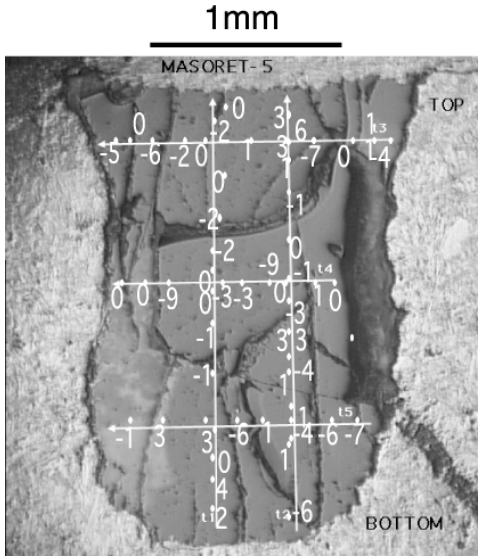

Soret Effect Calibration
(±10 ºC)

Thermocouple instability/drift

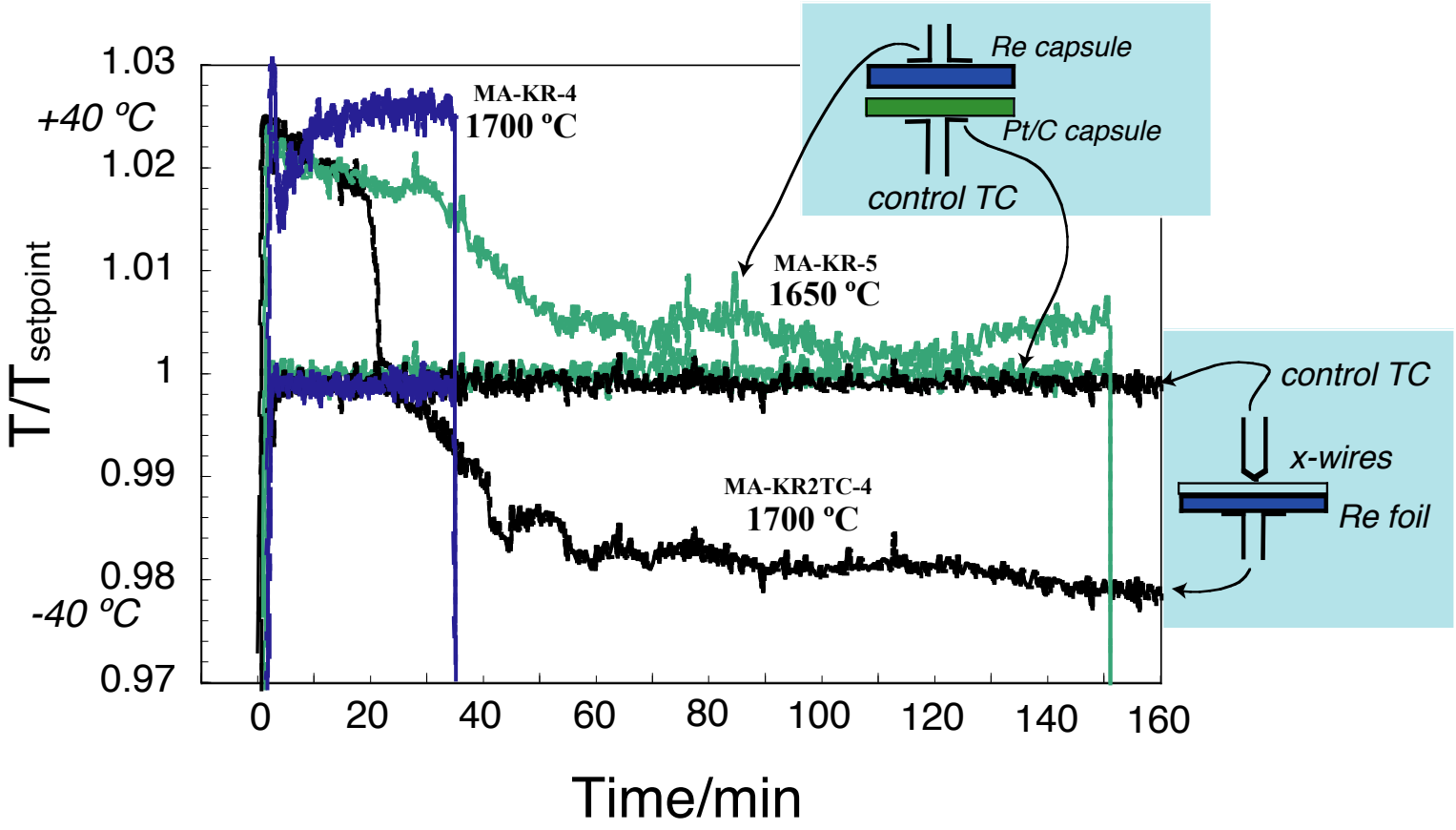

- Short-time-scale *instability* - stress relief, recrystallization
- Long-time-scale *drift* - volume diffusion, contamination, oxidation

(Lesher et al., 2003)

Pressure Calibration

Metal Transitions

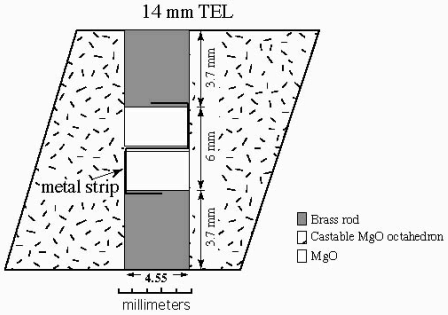

Useful Metal Transitions (Bean et al., 1986, Physica 139 &140B, 52-54)	*GPa*
Bi I-II	*2.550±0.006*
Tl II-III	*3.68±0.03*
Ba I-II	*5.5±0.1*
Bi (upper)	*7.7±0.2*
Sn	*9.4±0.3*
Ba (upper)	*12.3±0.5*
Pb	*13.4±0.6*

Figure 3. Cross-section of a metal transition assembly.

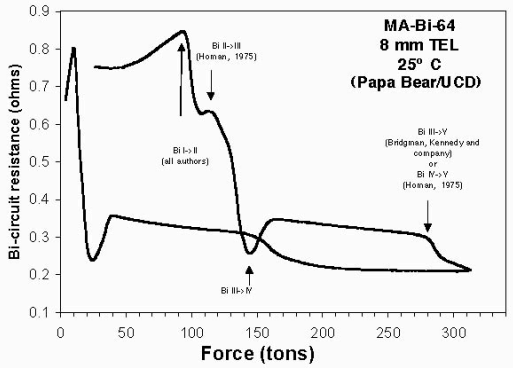

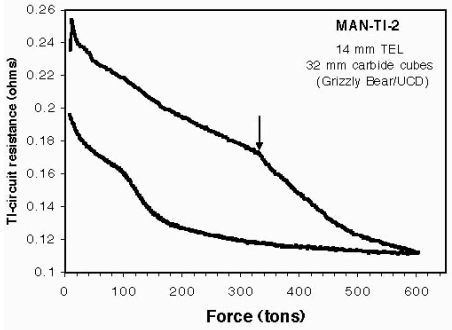

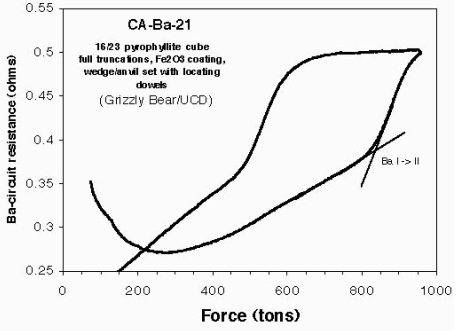

Phase Bracketing

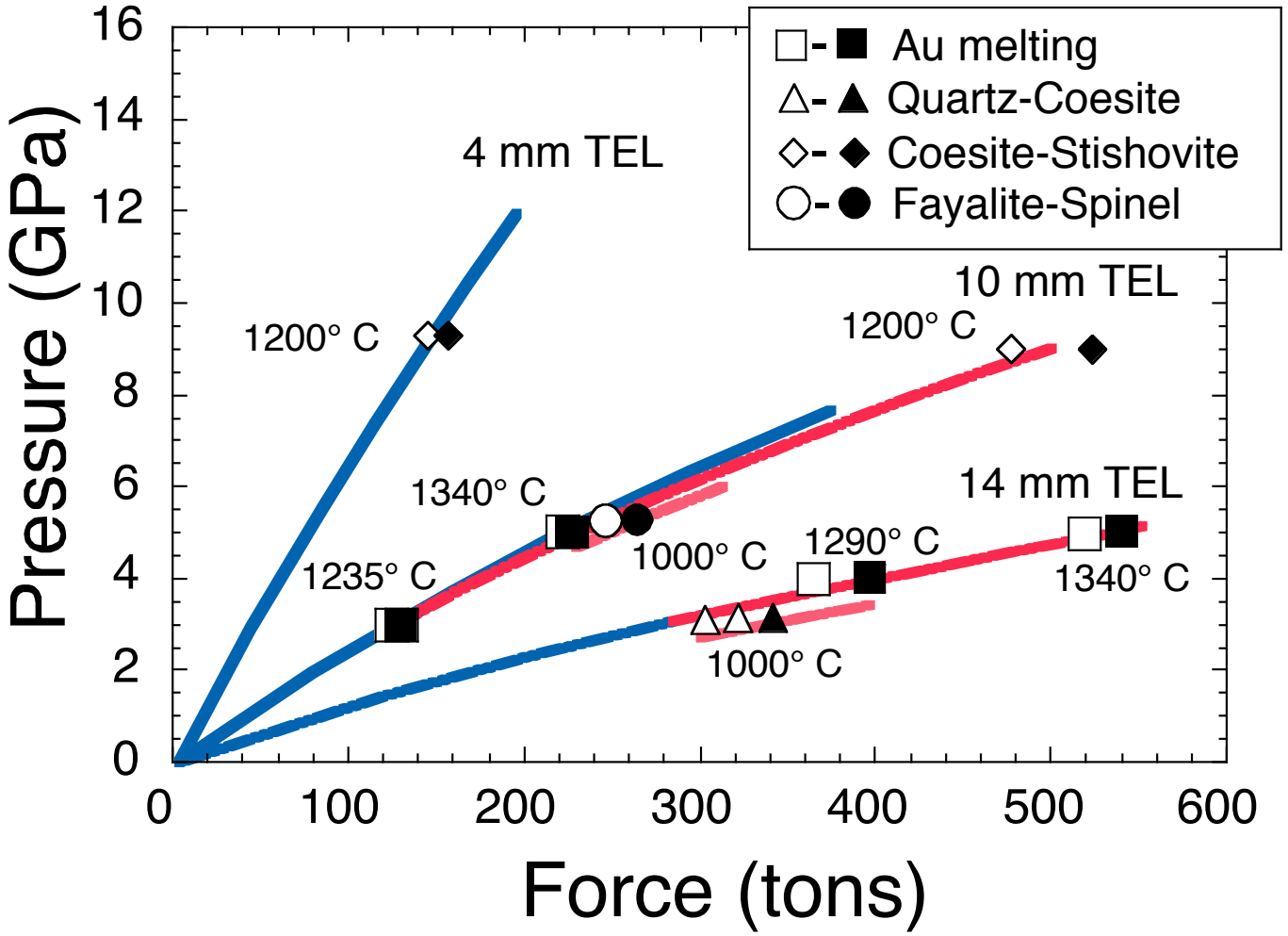

Phase Bracketing

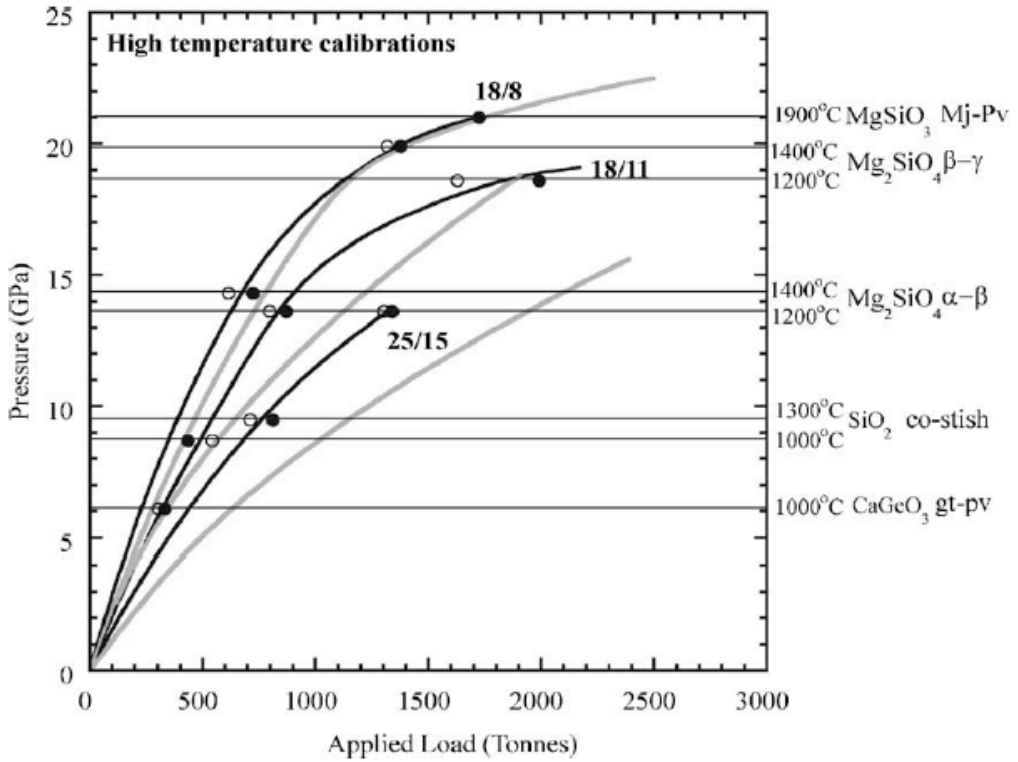

Fig. 4. High-temperature pressure calibration curves are shown (black lines). Room temperature calibrations (grey) plot below the high temperature curves of each assembly. The transformations on which the calibrations are based are $CaGeO_3$ garnet to perovskite (gt–pv), SiO_2 coesite to stishovite (co–stish), Mg_2SiO_4 forsterite to wadsleyite (α–β) and wadsleyite to ringwoodite (β–γ), and $MgSiO_3$ majorite to perovskite (Mj–Pv). The occurrence of either the high or low-pressure phase at each transformation is indicated by either filled or opened circles respectively.

EOS

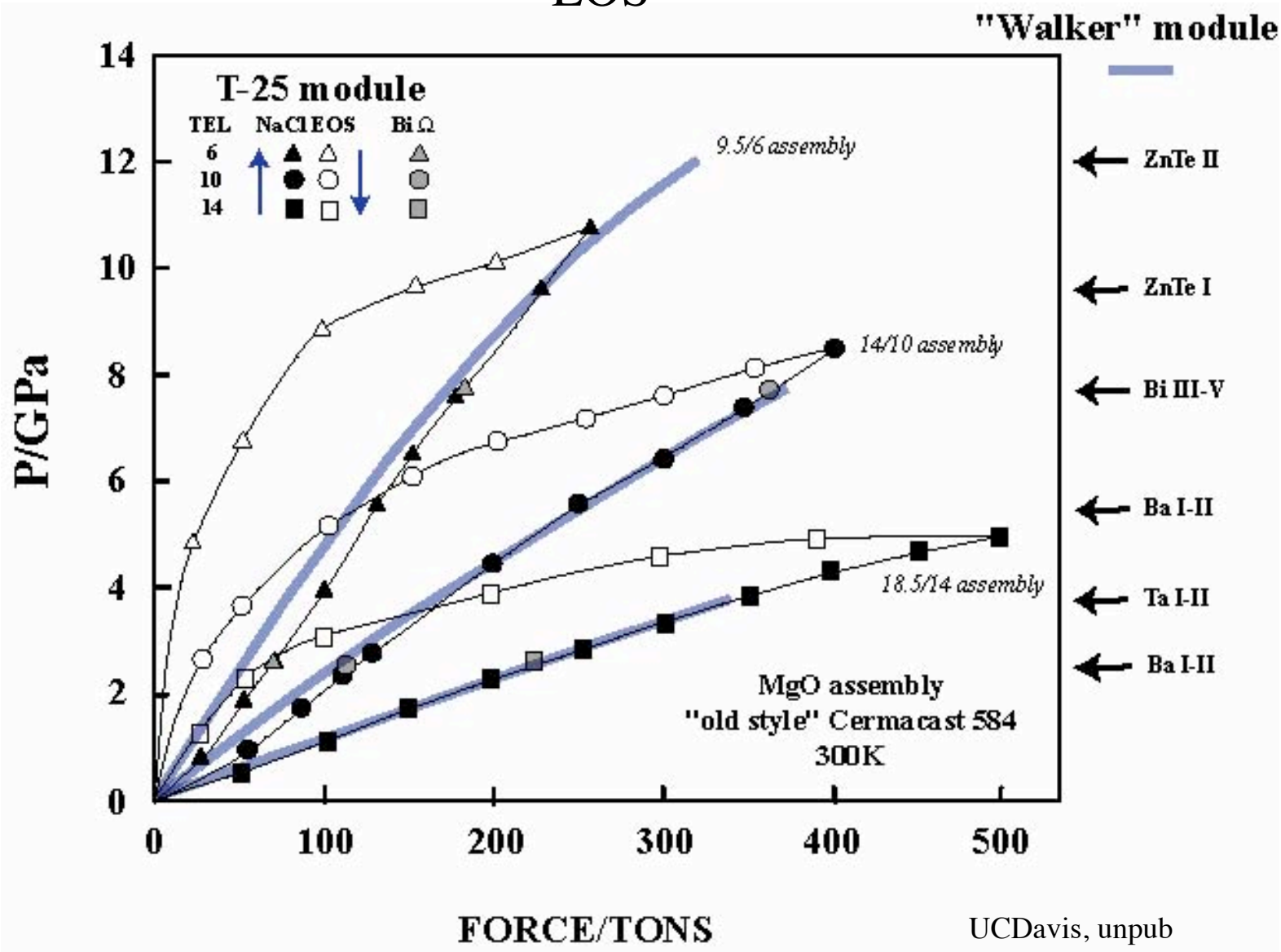

UCDavis, unpub

Let the fun begin!